

ADAPTIVE MODELING FOR FREE-SURFACE FLOWS*

SIMONA PEROTTO¹

Abstract. This work represents a first step towards the simulation of the motion of water in a complex hydrodynamic configuration, such as a channel network or a river delta, by means of a suitable “combination” of different mathematical models. In this framework a wide spectrum of space and time scales is involved due to the presence of physical phenomena of different nature. Ideally, moving from a hierarchy of hydrodynamic models, one should solve throughout the whole domain the most complex model (with solution u_{fine}) to accurately describe all the physical features of the problem at hand. In our approach instead, for a user-defined output functional \mathcal{F} , we aim to approximate, within a prescribed tolerance τ , the value $\mathcal{F}(u_{\text{fine}})$ by means of the quantity $\mathcal{F}(u_{\text{adapted}})$, u_{adapted} being the so-called adapted solution solving the simpler models on most of the computational domain while confining the complex ones only on a restricted region. Moving from the simplified setting where only two hydrodynamic models, fine and coarse, are considered, we provide an efficient tool able to automatically select the regions of the domain where the coarse model rather than the fine one are to be solved, while guaranteeing $|\mathcal{F}(u_{\text{fine}}) - \mathcal{F}(u_{\text{adapted}})|$ below the tolerance τ . This goal is achieved *via* a suitable *a posteriori* modeling error analysis developed in the framework of a goal-oriented theory. We extend the dual-based approach provided in [Braack and Ern, *Multiscale Model Sim.* **1** (2003) 221–238], for steady equations to the case of a generic time-dependent problem. Then this analysis is specialized to the case we are interested in, *i.e.* the free-surface flows simulation, by emphasizing the crucial issue of the time discretization for both the primal and the dual problems. Finally, in the last part of the paper a widespread numerical validation is carried out.

Mathematics Subject Classification. 65J15, 65M15, 65M60.

Received: October 21, 2004.

1. INTRODUCTION

The study of free-surface flows comprises a wide range of physical phenomena, from tidal flows, to water motion in large basins, river courses, channels, etc. Ideally, one should solve the full 3D Navier-Stokes equations to capture all the physical features of the problem at hand. However, this approach requires a huge computational effort. In order to reduce such a computational cost, a hierarchy of simplified hydrodynamic models has been proposed in the literature (see, *e.g.*, [33, 36, 37]).

Keywords and phrases. Modeling adaptivity, *a posteriori* error estimate, goal-oriented analysis, free-surface flows, dual problem, finite elements.

* This work has been supported by the GNCS Project “Numerical Methods for multiscale evolutionary problems”.

¹ MOX-Modeling and Scientific Computing, Department of Mathematics “F. Brioschi”, Politecnico of Milano, via Bonardi 9, 20133 Milano, Italy. simona.perotto@mate.polimi.it

© EDP Sciences, SMAI 2006

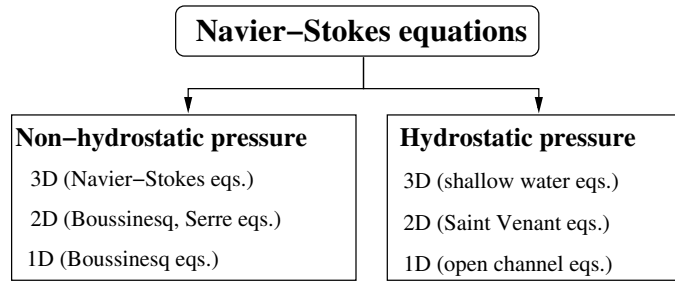


FIGURE 1. A possible classification of the most widespread hydrodynamic models.

Essentially we can distinguish among models of different dimension (1D, 2D and 3D) and models of different physical nature, that is, derived under physical assumptions of various type. According to a dimensional classification, for the 3D case we can consider the free-surface Navier-Stokes or the hydrostatic shallow water equations; concerning the 2D situation, the Boussinesq, Serre or Saint-Venant equations can be adopted; finally, in the one-dimensional case, the 1D counterparts of these latter models are usually employed. From a physical viewpoint, non-hydrostatic models (Boussinesq and Serre equations) are generally opposed to the hydrostatic ones (Saint-Venant equations) (see Fig. 1). The approach proposed in this paper consists of a suitable coupling of some of the models mentioned above, by solving the most expensive one only in the regions of the domain where it is strictly necessary. One can decide to couple free-surface models of different dimension or models of the same dimension but different from a physical (or analytical) viewpoint. According to the model coupling classification proposed in [26], the first choice coincides with a *dimensionally heterogeneous-physically homogeneous* coupling, while in the second case a *dimensionally homogeneous-physically heterogeneous* coupling is performed.

Whatever approach is adopted, the crucial matter is: where are we allowed to use the simpler model and where do we have to solve the more complex one? One can make this choice *a priori*, moving, for instance, from physical considerations or, alternatively, driven by a suitable *a posteriori* modeling error estimator able to automatically detect the regions where each model can be more conveniently employed. However, if the *a priori* approach is rather widespread (just think about the classical domain decomposition theory [13, 31, 32], or the geometrical multiscale approach investigated in [14, 15]), the *a posteriori* analysis represents a very recent area of interest, so far essentially confined to dimensionally homogeneous couplings and to the modeling of heterogeneous materials [1, 27–30, 34].

Concerning our investigation in the free-surface flows framework, in [25, 26] we exploit an *a priori* geometrical multiscale strategy to couple the 2D and the 1D shallow water equations, suitable matching conditions between the two models being derived. Moving from the corresponding numerical results we can state that if the considered hydrodynamic configuration is simple (*e.g.*, a straight channel or a river bifurcation) then this approach turns out to be reliable. On the contrary, in the presence of a more complex configuration (for instance, a channel with an obstacle), the accuracy of the approximate solution can be often preserved only by solving the dimensionally higher model on a large portion of the domain.

On the other hand, this paper is meant as a first step in view of an automatic tool able to drive a realistic simulation of the motion of water in a complex hydrodynamic system, by selecting the regions of the domain where the different models have to be solved. Since this is a preliminary work, we limit the analysis to the coupling of two-dimensional equations belonging to the same family of hydrodynamic models (Saint-Venant like equations), *i.e.* to hyperbolic equations sharing the same functional space and boundary conditions. We also aim to measure the influence of the model on a user-defined output functional \mathcal{F} *via* the resolution of a proper dual problem. This approach is a generalization to the modeling error analysis of the well-known *dual-weighted residual* (DWR) method provided in [7] for the *a posteriori* discretization error control. In particular, we extend the analysis in [9] for steady equations to the case of a generic time-dependent problem, while particularizing it to the application we are interested in, that is the free-surface flows simulation. The main difficulty related to

the unsteady setting is an efficient management of the time discretization of both the primal and dual problems, the time scales reversing one another. The proposed analysis has been successfully tested on some standard hydrodynamics configurations (channels and river bifurcations). As natural follow-up in view of a more thorough simulation, a coupling among several hydrodynamic models is desirable (see also Sect. 6 for further research hints).

The outline of the paper is as follows. In Section 2 we provide a modeling *a posteriori* error analysis moving from a general unsteady setting. Then, in Section 3, this analysis is particularized to the free-surface flows framework. Section 4 is devoted to the numerical discretization. In Section 5 a sound numerical validation of the proposed analysis is carried out, first by introducing the adaptive procedure and then by assessing it on some test cases. Finally some conclusions and perspectives are drawn in Section 6.

2. MODELING ERROR ANALYSIS FOR UNSTEADY PROBLEMS

This analysis can be set in the framework of a goal-oriented adaptivity. Let \mathcal{F} be the output functional we are interested in, possibly nonlinear. Standard examples of meaningful functionals in computational fluid dynamics (CFD) are the lift and drag around bodies in external flows or mean and local values. We aim to measure the influence of the model on \mathcal{F} by solving a suitable dual problem.

In more detail, let us assume we have at our disposal two time-dependent models, the *fine* model and the *coarse* one, with solution u_{fine} and u_{coarse} , respectively. Our goal is twofold. First we aim to approximate the goal value $\mathcal{F}(u_{\text{fine}})$ by means of the quantity (cheaper to be computed) $\mathcal{F}(u_{\text{adapted}})$, u_{adapted} being the solution of an “intermediate” problem obtained by solving the fine model on a restricted area of the domain only. Second, we look for an automatic tool able to detect, *via* a model adaption procedure, the regions of the domain where, at each time, the two models, fine and coarse, have to be solved, so that the quantity $|\mathcal{F}(u_{\text{fine}}) - \mathcal{F}(u_{\text{adapted}})|$ be under a prescribed tolerance, while minimizing the computational cost. This task is achieved *via* a suitable *a posteriori* modeling error analysis, generalizing to the unsteady case the dual-based approach proposed in [9]. Let us detail now the derivation of this analysis.

Throughout we use a standard notation to denote the Sobolev spaces of functions with Lebesgue measurable derivatives, and the corresponding norms [21].

Let $Q = \Omega \times (0, T]$ be the considered space-time domain, with Ω an open (regular) bounded set of \mathbb{R}^2 and $T > 0$. Let us introduce the following *family* of primal problems in variational formulation: find $u_\alpha \in V$ such that

$$\left(\frac{\partial u_\alpha}{\partial t}, \psi \right) + a(u_\alpha)(\psi) + d(u_\alpha)(\alpha\psi) = (f, \psi), \quad \text{for any } \psi \in V, \quad (1)$$

with $u_\alpha(0) = u_\alpha^0$ the initial datum, and with $f \in L^2(Q)$ a given function. Here V is a suitable space-time functional space accounting for the boundary conditions associated with the problem at hand, while (\cdot, \cdot) is the standard $L^2(Q)$ -scalar product. The quantities $a(u_\alpha)(\cdot)$ and $d(u_\alpha)(\cdot)$ in (1) denote semilinear forms, *i.e.* they are linear with respect to the second argument but *may be* nonlinear in u_α . Moreover, let us assume the form $d(u_\alpha)(\cdot)$ to be “trickier” than $a(u_\alpha)(\cdot)$ from an analytical viewpoint (for instance a nonlinear term with respect to u_α).

The parameter $\alpha = \alpha(\mathbf{x}, t) \in L^\infty(Q)$ in (1), with $\mathbf{x} = (x, y)^T \in \Omega$ and $t \in (0, T]$, is a function, piecewise constant on a given partition of Q in subdomains Q_i and taking on the values 0 and 1 only. In view of the discrete formulation, the partition $\{Q_i\}$ of Q can be identified with the computational space-time grid.

In particular, the choice $\alpha = 1$ everywhere yields the *fine* problem (*i.e.* the most expensive one to be approximated), while for α identically equal to zero we switch to the *coarse* model (*i.e.* to the cheapest one). In practice, at each time t_j , according to the information provided by the modeling error estimator we are looking for, we compute the solution of an intermediate primal problem (1) with the trickier part $d(u_\alpha)(\psi)$ “active” only in the subdomains Q_i of Q where $\alpha(\mathbf{x}, t_j) = 1$, with $\mathbf{x} \in \Omega$. Notice that, even if we get rid of the semilinear form $d(u_\alpha)(\psi)$ in some areas of the domain, we are neither changing the differential nature of problem (1) nor the associated boundary conditions. Thus the functional space V is the same for each model of the family (1).

Remark 2.1. The choice of the coarse model can be driven by different strategies. Ideally, a hierarchy of models describing the phenomenon we are interested in should be available. Then, one can choose a coarse model simpler, for instance, from an analytical point of view (a coarse linear problem instead of a fine nonlinear one) or from a physical viewpoint (*e.g.*, a mathematical model derived under simplifying physical hypotheses). For instance, in the elasticity framework, the most recurrent choice consists of substituting the elasticity tensor (usually a highly oscillatory function of the position) with a regularized elasticity tensor (see [27–30]). In Section 3 we specify the criterion adopted in the free-surface flows setting.

Let us begin by analyzing the *fine* primal problem. The corresponding variational formulation is given by (1) with $\alpha = 1$, and reads as: find $u_1 \in V$ such that

$$\left(\frac{\partial u_1}{\partial t}, \psi\right) + a(u_1)(\psi) + d(u_1)(\psi) = (f, \psi), \quad \text{for any } \psi \in V, \quad (2)$$

with $u_1(0) = u_1^0$ the initial datum.

Let us assume that the solution u_1 of (2) exists unique in V . This hypothesis allows us to introduce the following (trivial) constrained minimization problem, according to an optimal control approach [7]: find $u_1 \in V$ such that

$$\mathcal{F}(u_1) = \inf_{v \in M} \mathcal{F}(v), \quad (3)$$

where

$$M = \left\{ v \in V : \left(\frac{\partial v}{\partial t}, \xi\right) + a(v)(\xi) + d(v)(\xi) = (f, \xi), \text{ for any } \xi \in V, \text{ and with } v(0) = u_1^0 \right\},$$

and $\mathcal{F} : V \rightarrow \mathbb{R}$ is the chosen goal functional. The triviality of (3) is due to the fact that the space M consists of one element only, that is $M = \{u_1\}$, where u_1 is the solution of (2). Thus solving (2) is equivalent to solving (3) for the unknown u_1 . On the other hand, the reformulation of (2) as a constrained optimization problem allows us to use the Lagrangian technique to impose the constraint. With this aim, we introduce the *fine* Lagrangian $L : V \times V = X \rightarrow \mathbb{R}$ defined by

$$L(x_1) = \mathcal{F}(u_1) + (f, z_1) - a(u_1)(z_1) - d(u_1)(z_1) - \left(\frac{\partial u_1}{\partial t}, z_1\right), \quad (4)$$

with $x_1 = (u_1, z_1) \in X$ and where z_1 is the so-called Lagrange multiplier (or influence function) associated with the functional \mathcal{F} . Notice that, due to its definition, the Lagrangian L turns out to be a semilinear form as well as $a(u_1)(\cdot)$ and $d(u_1)(\cdot)$. By definition the minimum point of (3) coincides with the first component of the saddle-point x_1 of (4), so that we are interested in finding the critical points $x_1 \in X$ of L , satisfying

$$L'(x_1)(y) = 0, \quad \text{for any } y = (\varphi, \psi) \in X, \quad (5)$$

where

$$L'(x_1)(y) = \mathcal{F}'(u_1)(\varphi) - a'(u_1)(\varphi, z_1) - d'(u_1)(\varphi, z_1) - \left(\frac{\partial \varphi}{\partial t}, z_1\right) + (f, \psi) - a(u_1)(\psi) - d(u_1)(\psi) - \left(\frac{\partial u_1}{\partial t}, \psi\right) \quad (6)$$

denotes the derivative of the fine Lagrangian L applied to the test function y . Notice that in (6) we resort to a Gâteaux differentiation [23], so that the semilinear forms

$$\mathcal{F}'(u_1)(\varphi) = \lim_{\theta \rightarrow 0} \frac{1}{\theta} \{ \mathcal{F}(u_1 + \theta\varphi) - \mathcal{F}(u_1) \}, \tag{7}$$

$$a'(u_1)(\varphi, z_1) = \lim_{\theta \rightarrow 0} \frac{1}{\theta} \{ a(u_1 + \theta\varphi)(z_1) - a(u_1)(z_1) \}, \tag{8}$$

$$d'(u_1)(\varphi, z_1) = \lim_{\theta \rightarrow 0} \frac{1}{\theta} \{ d(u_1 + \theta\varphi)(z_1) - d(u_1)(z_1) \} \tag{9}$$

are linear with respect to φ and z_1 but preserve the (possible) nonlinearity in u_1 .

Due to the independence of the test functions ψ and φ and *via* (5)-(6), the minimization problem (3) reduces to looking for $x_1 = (u_1, z_1) \in X$ such that

$$\left(\frac{\partial u_1}{\partial t}, \psi \right) + a(u_1)(\psi) + d(u_1)(\psi) = (f, \psi), \quad \text{for any } \psi \in V, \tag{10}$$

$$\left(\frac{\partial \varphi}{\partial t}, z_1 \right) + a'(u_1)(\varphi, z_1) + d'(u_1)(\varphi, z_1) = \mathcal{F}'(u_1)(\varphi), \quad \text{for any } \varphi \in V. \tag{11}$$

We recognize in (10) the variational formulation (2) of the fine primal problem, while equation (11) coincides with the (fine) dual problem associated with (2), and corresponding to the choice \mathcal{F} for the goal quantity. Notice that the dual problem (11) is linear with respect to the influence function z_1 . Moreover it will be completed with a suitable final condition, $z_1(T) = z_1^T$, the time scale being reverse in the dual setting.

Now, let us identify equation (1) with the variational formulation of the *adapted* primal problem.

The (trivial) constrained minimization problem (3) is thus replaced by the new one: find $u_\alpha \in V$ such that

$$\mathcal{F}(u_\alpha) = \inf_{v \in M_\alpha} \mathcal{F}(v), \tag{12}$$

where

$$M_\alpha = \left\{ v \in V : \left(\frac{\partial v}{\partial t}, \xi \right) + a(v)(\xi) + d(v)(\alpha\xi) = (f, \xi), \text{ for any } \xi \in V, \text{ and with } v(0) = u_\alpha^0 \right\}.$$

By exactly mimicking the fine analysis, we introduce the *adapted* Lagrangian

$$L_\alpha(x_\alpha) = \mathcal{F}(u_\alpha) + (f, z_\alpha) - a(u_\alpha)(z_\alpha) - d(u_\alpha)(\alpha z_\alpha) - \left(\frac{\partial u_\alpha}{\partial t}, z_\alpha \right), \tag{13}$$

$x_\alpha = (u_\alpha, z_\alpha) \in X$ and z_α being the saddle point of L_α and the Lagrange multiplier associated with the functional \mathcal{F} , respectively. Thus the minimization problem (12) leads us to the resolution of the adapted primal problem (1) and of the adapted dual problem

$$\left(\frac{\partial \varphi}{\partial t}, z_\alpha \right) + a'(u_\alpha)(\varphi, z_\alpha) + d'(u_\alpha)(\varphi, \alpha z_\alpha) = \mathcal{F}'(u_\alpha)(\varphi), \quad \text{for any } \varphi \in V, \tag{14}$$

$z_\alpha(T) = z_\alpha^T$ being the corresponding final datum.

Remark 2.2. The dual problems (11) and (14) have to be provided with suitable boundary conditions. In the steady case and for an output functional \mathcal{F} consisting of an integral over the whole domain Ω and of an integral on the boundary $\partial\Omega$ of the domain, the dual boundary conditions can be rigorously identified according to the analysis in [16]. In the model adaption framework, a first attempt in such a direction is performed in [11]

for the simple case of the one-dimensional Helmholtz equation. As alternative approach, in the presence of a time-dependent problem or for a more complex functional \mathcal{F} , the boundary conditions to be associated with the dual problem can be derived *via* the *Lagrange identity* [22]. The strategy pursued in the free-surface flows framework is again different, due to the adopted constrained minimization setting *via* the Lagrange multipliers (see Sect. 3.2).

In the sequel the notations are often shortened moving from the trivial relation between the fine L and the adapted L_α Lagrangians, given by

$$L(x) = L_\alpha(x) + \delta L(x), \quad \text{for any } x = (u, z) \in X, \tag{15}$$

with

$$\delta L(x) = -d(u)((1 - \alpha)z). \tag{16}$$

With the aim of keeping the quantity $|\mathcal{F}(u_1) - \mathcal{F}(u_\alpha)|$ below a prescribed tolerance, let us first remark that, thanks to (2) and (1), relations (4) and (13) provide us with the exact values

$$\mathcal{F}(u_1) = L(x_1) \quad \text{and} \quad \mathcal{F}(u_\alpha) = L_\alpha(x_\alpha), \tag{17}$$

i.e. $\mathcal{F}(u_1)$ and $\mathcal{F}(u_\alpha)$ coincide with the values of the fine and of the adapted Lagrangians at the stationary points x_1 and x_α , respectively. On the other hand, we would like to skip the approximation of the fine problem: thus we look for an approximation of the quantity $\mathcal{F}(u_1) - \mathcal{F}(u_\alpha)$ in terms of easily computable quantities, *i.e.* of the problem data and of the adapted solutions u_α and z_α only. With this aim, let us define the *modeling residuals* $\rho_M(u_\alpha)(\cdot)$ and $\bar{\rho}_M(u_\alpha)(\cdot, z_\alpha)$ associated with the fine primal and with the fine dual problem, respectively, given by

$$\begin{aligned} \rho_M(u_\alpha)(\psi) &= (f, \psi) - \left(\frac{\partial u_\alpha}{\partial t}, \psi\right) - a(u_\alpha)(\psi) - d(u_\alpha)(\psi) \\ &= -d(u_\alpha)((1 - \alpha)\psi), \quad \text{for any } \psi \in V, \end{aligned} \tag{18}$$

$$\begin{aligned} \bar{\rho}_M(u_\alpha)(\varphi, z_\alpha) &= \mathcal{F}'(u_\alpha)(\varphi) - \left(\frac{\partial \varphi}{\partial t}, z_\alpha\right) - a'(u_\alpha)(\varphi, z_\alpha) - d'(u_\alpha)(\varphi, z_\alpha) \\ &= -d'(u_\alpha)(\varphi, (1 - \alpha)z_\alpha), \quad \text{for any } \varphi \in V. \end{aligned} \tag{19}$$

Notice that the residuals $\rho_M(u_\alpha)(\psi)$ and $\bar{\rho}_M(u_\alpha)(\varphi, z_\alpha)$ measure the level to which the adapted solutions u_α and z_α fail to satisfy the fine problems (10) and (11), respectively. In the sequel we will refer to them as primal and dual modeling residual.

The modeling error analysis in [9] can be generalized to the case of non-stationary problems, as stated in the following result:

Proposition 2.3. *Let us assume that the semilinear forms $a(u_\alpha)(\cdot)$ and $d(u_\alpha)(\cdot)$ and the functional \mathcal{F} are sufficiently differentiable with respect to u_α , for any $\alpha \in L^\infty(Q)$. Then we have*

$$\mathcal{F}(u_1) - \mathcal{F}(u_\alpha) = \underbrace{\rho_M(u_\alpha)(z_\alpha)}_{\text{(I)}} + \underbrace{\frac{1}{2}\{\rho_M(u_\alpha)(e_z) + \bar{\rho}_M(u_\alpha)(e_u, z_\alpha)\}}_{\text{(II)}} + \underbrace{R}_{\text{(III)}}, \tag{20}$$

where the modeling residuals are defined according to (18) and (19), $e_u = u_1 - u_\alpha$ and $e_z = z_1 - z_\alpha$ are the primal and the dual error, respectively, while

$$R = \frac{1}{2} \int_0^1 L'''(x_\alpha + se)(e, e, e)s(s - 1) ds, \tag{21}$$

is a remainder term, with $e = (e_u, e_z) = x_1 - x_\alpha$.

Proof. The proof of Theorem 2.1 in [9] can be extended to the unsteady problems (1) and (2). The time derivatives in the definition of the Lagrangians are not troublesome for the proof: the explicit definitions of L and L_α are never involved, relations (15) and (16) being essentially exploited. Thus we easily prove that

$$\mathcal{F}(u_1) - \mathcal{F}(u_\alpha) = -d(u_\alpha)((1 - \alpha)z_\alpha) - \frac{1}{2} \left\{ d(u_\alpha)((1 - \alpha)e_z) + d'(u_\alpha)(e_u, (1 - \alpha)z_\alpha) \right\} + R,$$

i.e. relation (20) after substituting the modeling residuals $\rho_M(u_\alpha)(z_\alpha)$, $\rho_M(u_\alpha)(e_z)$ and $\bar{\rho}_M(u_\alpha)(e_u, z_\alpha)$, according to the definitions (18) and (19). \square

For the reader's ease we provide the complete proof of result (20) in the Appendix.

Notice that, at this stage, result (20) provides us with an exact expression for the quantity $\mathcal{F}(u_1) - \mathcal{F}(u_\alpha)$. Nevertheless it involves quantities depending on the fine solutions, *i.e.* the primal and dual errors e_u and e_z . Thus, after neglecting the remainder term R , error estimates for e_u and e_z , in terms of computable quantities, should be found to make "operative" relation (20). This is the approach followed, for instance, in [27–30]. However estimates of this type cannot be easily derived for any differential problem. Saint-Venant equations provide an example in such a direction. As alternative way to make the right-hand side of (20) useful in practice, one can introduce suitable simplifying assumptions on the problem at hand (see [9]). We adopt this second strategy. In more detail, we first demand for a *stability property* of the functional $L'(x)$, by assuming the existence of a constant $\beta > 0$ such that, for any x_n and $x_m \in X$,

$$\|x_n - x_m\|_X \leq \beta \|L'(x_n) - L'(x_m)\|_{X'}, \quad (22)$$

$\|\cdot\|_X$ and $\|\cdot\|_{X'}$ denoting the norms associated with the space X and its dual X' , respectively. Notice that inequality (22) essentially guarantees the invertibility of $L'(x)$.

Then we assume that, for any $u \in V$, the semilinear form $d(u)(\cdot)$ and its derivatives are sufficiently small. This last request, combined with (22) and thanks to (5), (15) and the relation $L'_\alpha(x_\alpha)(y) = 0$, for any $y \in X$, guarantees that

$$\|e\|_X = \|x_1 - x_\alpha\|_X \leq \beta \|L'(x_1) - L'(x_\alpha)\|_{X'} = \beta \|\delta L'(x_\alpha)\|_{X'} \leq \beta C(d) \|x_\alpha\|_X,$$

with $C(d) \ll 1$, *i.e.* that $e = O(C(d))$. By studying the order of magnitude of the quantities (I), (II) and (III) in (20) in terms of $C(d)$, we get that (I) = $O(C(d))$, while (II) = $O([C(d)]^2)$, and (III) = $O([C(d)]^3)$. These considerations allow us to neglect the terms (II) and (III) in (20), *i.e.* to estimate the goal quantity $\mathcal{F}(u_1) - \mathcal{F}(u_\alpha)$ as

$$\mathcal{F}(u_1) - \mathcal{F}(u_\alpha) \simeq \eta_\alpha = \rho_M(u_\alpha)(z_\alpha) = -d(u_\alpha)((1 - \alpha)z_\alpha).$$

The quantity η_α represents the desired *a posteriori modeling error estimator*, being expressed in terms of computable quantities only. It will suggest us where the fine problem rather than the coarse one has to be solved on the computational domain to guarantee the quantity $|\mathcal{F}(u_1) - \mathcal{F}(u_\alpha)|$ below a prescribed tolerance τ . In Section 5 we detail the procedure pursued with this aim.

Remark 2.4. In Section 5.2 we verify numerically the considerations made above on the order of magnitude of the terms (I) and (II), moving from some hydrodynamic configurations of interest. This will partially strengthen the requirements made above on the functional $L'(x)$ and on the semilinear form $d(u)(\cdot)$ together with its derivatives.

Remark 2.5. A third approach, alternative to the ones proposed in [9, 27–30], to make the quantity (I) + (II) in (20) computable, is now under investigation, even if it sounds not generalizable in a straightforward way to any differential problem, as well as the analysis in [27–30] (see also Sect. 6).

Remark 2.6. The analysis above holds also if $\Omega \subset \mathbb{R}^3$. The choice of the two-dimensional framework is only dictated by the software available for our numerical tests.

3. FREE-SURFACE FLOWS SIMULATION

In this section we aim to specialize the *a posteriori* modeling error analysis provided in Section 2 to the application we are interested in, that is the free-surface flows simulation. As already pointed out, due to the preliminary character of this work, we choose the simple setting where two hyperbolic models, sharing the same functional space and boundary conditions, are coupled. The idea is to generalize the analysis below to the coupling among several hydrodynamics models, in view of realistic simulations [24].

Let us consider the hierarchy of free-surface flows models

$$\begin{cases} \frac{\partial \mathbf{u}_\alpha}{\partial t} + \alpha (\mathbf{u}_\alpha \cdot \nabla) \mathbf{u}_\alpha + g \nabla h_\alpha = 0 & \text{with } (\mathbf{x}, t) \in Q, \\ \frac{\partial h_\alpha}{\partial t} + \nabla \cdot (h_\alpha \mathbf{u}_\alpha) = 0 & \text{with } (\mathbf{x}, t) \in Q, \end{cases} \quad (23)$$

with $\mathbf{u}_\alpha(0) = \mathbf{u}_\alpha^0$, $h_\alpha(0) = h_\alpha^0$ the initial data, g the gravity acceleration and where the unknowns \mathbf{u}_α and h_α denote the mean velocity and the total water depth, respectively, while Q and the function α are defined as in Section 2. As α takes on the values 0 and 1 only, at each time t_j , the nonlinear convective term in the momentum equation will be “switched-on” only in the regions Q_i of Q where $\alpha(\mathbf{x}, t_j) = 1$, with $\mathbf{x} \in \Omega$, that is, ideally, only where the nonlinear advective features of the problem at hand significantly influence the target functional \mathcal{F} . Moreover, proper boundary conditions will be supplied to the hyperbolic system (23), depending on the hydrodynamic problem at hand (see Sect. 5.2 for more details).

According to the nomenclature of the previous section, we will refer to (23) as to the *adapted model*, *i.e.* the system solved in practice.

The choice $\alpha = 1$, for any $(\mathbf{x}, t) \in Q$, provides us with the *fine* model, that is with the Saint-Venant equations [36,37], written in the non-conservative form:

$$\begin{cases} \frac{\partial \mathbf{u}_1}{\partial t} + (\mathbf{u}_1 \cdot \nabla) \mathbf{u}_1 + g \nabla h_1 = 0 & \text{with } (\mathbf{x}, t) \in Q, \\ \frac{\partial h_1}{\partial t} + \nabla \cdot (h_1 \mathbf{u}_1) = 0 & \text{with } (\mathbf{x}, t) \in Q, \end{cases} \quad (24)$$

with $\mathbf{u}_1(0) = \mathbf{u}_1^0$, $h_1(0) = h_1^0$ the initial data. The absence of the forcing term in the momentum equation is due to the choice of considering only hydrodynamic configurations characterized by flat bottom and of neglecting the wind stress, the Coriolis force and the bottom friction.

From a computational viewpoint, system (24) is the most expensive one, the nonlinear term in the momentum equation being active on the whole domain. The expectation is to never solve the fine model everywhere but only on a reduced portion of Ω . This will be confirmed by the numerical validation in Section 5.2.

On the other hand, if α is identically equal to zero in Q , the adapted model reduces to the *coarse problem*

$$\begin{cases} \frac{\partial \mathbf{u}_0}{\partial t} + g \nabla h_0 = 0 & \text{with } (\mathbf{x}, t) \in Q, \\ \frac{\partial h_0}{\partial t} + \nabla \cdot (h_0 \mathbf{u}_0) = 0 & \text{with } (\mathbf{x}, t) \in Q. \end{cases} \quad (25)$$

Typically, also problem (25) will be never solved on the whole Ω . Were this the case, it could mean that the hydrodynamics involved in the problem at hand is simpler than what expected *a priori*, and the coarse model would suffice to reasonably describe the phenomenon.

To summarize, at each time t_j , neither the fine problem (24) nor the coarse one (25) will be solved on the whole Ω . The problem to be discretized will be the adapted model (23), according to the value of $\alpha(\mathbf{x}, t_j)$, for any $(\mathbf{x}, t_j) \in Q$.

Remark 3.1. The suppression of the nonlinear term in the momentum equation does not modify the hyperbolic character of the coarse model (25) as can be easily checked *via* a suitable characteristic analysis.

3.1. A modeling error estimator for shallow water equations

To derive a modeling error estimator working on the Saint-Venant like family of models (23), let us first fit these equations into the general framework of Section 2.

Let us move from the weak form associated with the fine problem (24): let us sum up the momentum and the continuity equations after multiplication by suitable test functions \mathbf{v} and q , respectively. This leads to the following formulation: find $(\mathbf{u}_1, h_1) \in \mathcal{W} = \mathcal{V} \times \mathcal{Z}$ such that

$$\left(\frac{\partial \mathbf{u}_1}{\partial t}, \mathbf{v} \right) + \left(\frac{\partial h_1}{\partial t}, q \right) + ((\mathbf{u}_1 \cdot \nabla) \mathbf{u}_1, \mathbf{v}) + g (\nabla h_1, \mathbf{v}) + (\nabla \cdot (h_1 \mathbf{u}_1), q) = 0, \quad \text{for any } (\mathbf{v}, q) \in \mathcal{W}, \quad (26)$$

with $\mathbf{u}_1(0) = \mathbf{u}_1^0$ and $h_1(0) = h_1^0$ the initial data. To simplify the weak form (26), we introduce the “global” unknown $U_1 = (\mathbf{u}_1, h_1) \in \mathcal{W}$ and test function $\Psi = (\mathbf{v}, q) \in \mathcal{W}$, so that we get: find $U_1 \in \mathcal{W}$ such that

$$\left(\frac{\partial U_1}{\partial t}, \Psi \right) + a(U_1)(\Psi) + d(U_1)(\Psi) = 0, \quad \text{for any } \Psi \in \mathcal{W}, \quad (27)$$

with $U_1(0) = U_1^0 = (\mathbf{u}_1^0, h_1^0)$ the initial data vector, and where

$$\left(\frac{\partial U_1}{\partial t}, \Psi \right) = \left(\frac{\partial \mathbf{u}_1}{\partial t}, \mathbf{v} \right) + \left(\frac{\partial h_1}{\partial t}, q \right)$$

while

$$a(U_1)(\Psi) = g (\nabla h_1, \mathbf{v}) + (\nabla \cdot (h_1 \mathbf{u}_1), q) \quad \text{and} \quad d(U_1)(\Psi) = ((\mathbf{u}_1 \cdot \nabla) \mathbf{u}_1, \mathbf{v})$$

are semilinear forms, linear with respect to Ψ but nonlinear in U_1 . Notice that, in this case, the forcing term in (2) is identically equal to zero.

Remark 3.2. The spaces \mathcal{V} and \mathcal{Z} depend on the boundary conditions associated with system (24), *i.e.* on the test case under examination. At this stage, we do not choose any specific boundary condition so that we can only state that \mathcal{V} and \mathcal{Z} are suitable subspaces of $[\mathbf{H}^1(\Omega)]^2$ and of $\mathbf{H}^1(\Omega)$, respectively.

Now let \mathcal{F} be the goal functional we are interested in. In the numerical results of Section 5.2 we identify \mathcal{F} with the kinetic energy and with the drag of the flow on the whole or on a subregion of the computational domain Ω or with the more challenging case of pointwise values. Following the constrained minimization procedure of Section 2, we first introduce the *fine* Lagrangian

$$L(\tilde{x}_1) = \mathcal{F}(U_1) - a(U_1)(Z_1) - d(U_1)(Z_1) - \left(\frac{\partial U_1}{\partial t}, Z_1 \right), \quad (28)$$

with $\tilde{x}_1 = (U_1, Z_1) \in \tilde{X} = \mathcal{W} \times \mathcal{W}$, and where $Z_1 = (\mathbf{w}_1, \kappa_1) \in \mathcal{W}$ is the vector of the Lagrange multipliers (or influence functions) associated with the functional \mathcal{F} . Thus, when looking for the stationary point \tilde{x}_1 of the Lagrangian L in (28), we are led to solving the fine primal problem (27) together with the corresponding dual one: find $Z_1 \in \mathcal{W}$ such that

$$\left(\frac{\partial \Phi}{\partial t}, Z_1 \right) + a'(U_1)(\Phi, Z_1) + d'(U_1)(\Phi, Z_1) = \mathcal{F}'(U_1)(\Phi), \quad \text{for any } \Phi \in \mathcal{W}, \quad (29)$$

with $Z_1(T) = Z_1^T = (\mathbf{w}_1^T, \kappa_1^T)$ the final data vector, and $\Phi = (\varphi, \vartheta)$ the test functions pair.

According to the Gâteaux derivative definition, we have that, for any $\Phi \in \mathcal{W}$,

$$\begin{aligned} a'(U_1)(\Phi, Z_1) &= g(\nabla\vartheta, \mathbf{w}_1) + (\nabla \cdot (h_1\varphi), \kappa_1) + (\nabla \cdot (\vartheta\mathbf{u}_1), \kappa_1), \\ d'(U_1)(\Phi, Z_1) &= ((\mathbf{u}_1 \cdot \nabla)\varphi, \mathbf{w}_1) + ((\varphi \cdot \nabla)\mathbf{u}_1, \mathbf{w}_1). \end{aligned}$$

Moreover, we remark that the components \mathbf{w}_1 and κ_1 of the dual solution Z_1 identify the dual mean velocity and the dual total water depth, respectively.

Now, let us move to the adapted model (23). By repeating the fine analysis, we introduce the adapted weak form: find $U_\alpha = (\mathbf{u}_\alpha, h_\alpha) \in \mathcal{W}$ such that

$$\left(\frac{\partial U_\alpha}{\partial t}, \Psi\right) + a(U_\alpha)(\Psi) + d(U_\alpha)(\alpha\Psi) = 0, \quad \text{for any } \Psi = (\mathbf{v}, q) \in \mathcal{W}, \quad (30)$$

with $U_\alpha(0) = U_\alpha^0 = (\mathbf{u}_\alpha^0, h_\alpha^0)$ the initial data vector, and where the scalar product $(\partial U_\alpha/\partial t, \Psi)$ and the semilinear forms $a(U_\alpha)(\cdot)$ and $d(U_\alpha)(\cdot)$ are defined as

$$\left(\frac{\partial U_\alpha}{\partial t}, \Psi\right) = \left(\frac{\partial \mathbf{u}_\alpha}{\partial t}, \mathbf{v}\right) + \left(\frac{\partial h_\alpha}{\partial t}, q\right) \quad (31)$$

and

$$a(U_\alpha)(\Psi) = g(\nabla h_\alpha, \mathbf{v}) + (\nabla \cdot (h_\alpha \mathbf{u}_\alpha), q) \quad \text{and} \quad d(U_\alpha)(\alpha\Psi) = ((\mathbf{u}_\alpha \cdot \nabla)\mathbf{u}_\alpha, \alpha\mathbf{v})$$

respectively. Via a minimization procedure, we are led to looking for the critical point $\tilde{x}_\alpha = (U_\alpha, Z_\alpha) \in \tilde{X}$ of the adapted Lagrangian

$$L_\alpha(\tilde{x}_\alpha) = \mathcal{F}(U_\alpha) - a(U_\alpha)(Z_\alpha) - d(U_\alpha)(\alpha Z_\alpha) - \left(\frac{\partial U_\alpha}{\partial t}, Z_\alpha\right),$$

i.e., to finding the solution $U_\alpha \in \mathcal{W}$ of the adapted primal problem (30) together with the solution $Z_\alpha = (\mathbf{w}_\alpha, \kappa_\alpha) \in \mathcal{W}$ of the associated dual problem: find $Z_\alpha \in \mathcal{W}$ such that

$$\left(\frac{\partial \Phi}{\partial t}, Z_\alpha\right) + a'(U_\alpha)(\Phi, Z_\alpha) + d'(U_\alpha)(\Phi, \alpha Z_\alpha) = \mathcal{F}'(U_\alpha)(\Phi), \quad \text{for any } \Phi \in \mathcal{W}, \quad (32)$$

with $Z_\alpha(T) = Z_\alpha^T = (\mathbf{w}_\alpha^T, \kappa_\alpha^T)$ the final data vector, $\Phi = (\varphi, \vartheta)$ the test functions pair, and where the scalar product $(\partial\Phi/\partial t, Z_\alpha)$ is defined according to (31) while the semilinear forms $a'(U_\alpha)(\cdot, Z_\alpha)$ and $d'(U_\alpha)(\cdot, \alpha Z_\alpha)$ are given by

$$\begin{aligned} a'(U_\alpha)(\Phi, Z_\alpha) &= g(\nabla\vartheta, \mathbf{w}_\alpha) + (\nabla \cdot (h_\alpha\varphi), \kappa_\alpha) + (\nabla \cdot (\vartheta\mathbf{u}_\alpha), \kappa_\alpha), \\ d'(U_\alpha)(\Phi, \alpha Z_\alpha) &= ((\mathbf{u}_\alpha \cdot \nabla)\varphi, \alpha\mathbf{w}_\alpha) + ((\varphi \cdot \nabla)\mathbf{u}_\alpha, \alpha\mathbf{w}_\alpha). \end{aligned}$$

Remark 3.3. Suitable boundary conditions have to be supplied to the dual problems (29) and (32). We refer to Section 3.2 for some general considerations about the choice of the dual boundary conditions and to Sections 5.2.1, 5.2.2 and 5.2.3 of the considered test cases for the corresponding specific choices.

We are now in a position to reformulate the result in Proposition 2.3 in the case of the hierarchy (23) of

free-surface flows models. With this aim, let us introduce the primal and the dual modeling residuals involved in (20):

$$\begin{aligned} \rho_M(U_\alpha)(Z_\alpha) &= -d(U_\alpha)((1-\alpha)Z_\alpha) = -((\mathbf{u}_\alpha \cdot \nabla)\mathbf{u}_\alpha, (1-\alpha)\mathbf{w}_\alpha), \\ \rho_M(U_\alpha)(E_Z) &= -d(U_\alpha)((1-\alpha)E_Z) = -((\mathbf{u}_\alpha \cdot \nabla)\mathbf{u}_\alpha, (1-\alpha)(\mathbf{w}_1 - \mathbf{w}_\alpha)), \\ \bar{\rho}_M(U_\alpha)(E_U, Z_\alpha) &= -d'(U_\alpha)(E_U, (1-\alpha)Z_\alpha) \\ &= -((\mathbf{u}_\alpha \cdot \nabla)(\mathbf{u}_1 - \mathbf{u}_\alpha), (1-\alpha)\mathbf{w}_\alpha) - (((\mathbf{u}_1 - \mathbf{u}_\alpha) \cdot \nabla)\mathbf{u}_\alpha, (1-\alpha)\mathbf{w}_\alpha), \end{aligned} \tag{33}$$

where $E_U = (\mathbf{u}_1 - \mathbf{u}_\alpha, h_1 - h_\alpha)$ and $E_Z = (\mathbf{w}_1 - \mathbf{w}_\alpha, \kappa_1 - \kappa_\alpha)$ are the primal and dual error, respectively. Proposition 2.3 thus reads as

Proposition 3.4. *If the functional \mathcal{F} is sufficiently differentiable with respect to U_α , for any $\alpha \in L^\infty(Q)$, then it holds that*

$$\mathcal{F}(U_1) - \mathcal{F}(U_\alpha) = \underbrace{\rho_M(U_\alpha)(Z_\alpha)}_{(I)} + \underbrace{\frac{1}{2}\{\rho_M(U_\alpha)(E_Z) + \bar{\rho}_M(U_\alpha)(E_U, Z_\alpha)\}}_{(II)} + \underbrace{R}_{(III)}, \tag{34}$$

the modeling residuals $\rho_M(U_\alpha)(Z_\alpha)$, $\rho_M(U_\alpha)(E_Z)$ and $\bar{\rho}_M(U_\alpha)(E_U, Z_\alpha)$ and the remainder term R being defined according to (33) and (21), with L given by (28), respectively.

To make result (34) effective from a computational viewpoint, we introduce the simplifying hypotheses of Section 2, by demanding the stability property (22) for the functional $L'(x)$, for any $x \in \tilde{X}$, together with proper regularity assumptions on $d(U)(\cdot)$ and on its derivatives, for any $U \in \mathcal{W}$. The desired shallow water modeling error estimator for the goal quantity $\mathcal{F}(U_1) - \mathcal{F}(U_\alpha)$ thus reads as

$$\mathcal{F}(U_1) - \mathcal{F}(U_\alpha) \simeq \eta_\alpha = \rho_M(U_\alpha)(Z_\alpha) = -((\mathbf{u}_\alpha \cdot \nabla)\mathbf{u}_\alpha, (1-\alpha)\mathbf{w}_\alpha). \tag{35}$$

Remark 3.5. As pointed out for the general unsteady setting, we could take advantage in (34) of suitable bounds for the errors E_U and E_Z , in terms of the adapted quantities U_α and Z_α , rather than resorting to the hypotheses above (see [27–30]). However, this task turns out to be not trivial for the shallow water equations, unless one moves from a conservative or viscous formulation of the shallow water system [3].

3.2. The dual problem: the boundary conditions matter

Let us move from the adapted dual problem, the fine analysis being recovered simply by choosing α identically equal to one. Looking for the dual boundary conditions we are obliged to move from the weak form (32) associated with the adopted constrained minimization approach. The strategy pursued in the sequel consists of deriving the differential form of the dual problem by suitably integrating by parts the corresponding weak form. Then the boundary terms yielded by this procedure are partially erased *via* the boundary conditions of the primal problem and in part exploited to get the desired dual boundary conditions. The idea is to get rid of all the boundary terms by suitably choosing the primal and the dual boundary conditions, as no boundary term appears in the weak form (32). Since this last step is strictly related to the considered test case, we refer to the Sections 5.2.1, 5.2.2 and 5.2.3 for the choice of the specific boundary conditions, while providing here the general analysis leading to the differential adapted dual problem.

As we aim to identify the differential form of both the momentum and the continuity dual equations, let us begin by highlighting the corresponding contribution in the weak form (32): the momentum equation is given by

$$\left(\frac{\partial \varphi}{\partial t}, \mathbf{w}_\alpha\right) + (\nabla \cdot (h_\alpha \varphi), \kappa_\alpha) + ((\mathbf{u}_\alpha \cdot \nabla)\varphi, \alpha \mathbf{w}_\alpha) + ((\varphi \cdot \nabla)\mathbf{u}_\alpha, \alpha \mathbf{w}_\alpha) = (\mathbf{g}_1, \varphi), \tag{36}$$

while the continuity one turns out to be

$$\left(\frac{\partial \vartheta}{\partial t}, \kappa_\alpha\right) + g(\nabla \vartheta, \mathbf{w}_\alpha) + (\nabla \cdot (\vartheta \mathbf{u}_\alpha), \kappa_\alpha) = (g_2, \vartheta), \quad (37)$$

$\mathbf{g}_1 = \mathbf{g}_1(\mathbf{u}_\alpha, h_\alpha)$ and $g_2 = g_2(\mathbf{u}_\alpha, h_\alpha)$ being the densities associated with the functional $\mathcal{F}'(U_\alpha)(\Phi)$. Let us move from the momentum equation and let us write out the primal and the dual velocity \mathbf{u}_α and \mathbf{w}_α , together with the test function φ , in terms of their x - and y -components, as $\mathbf{u}_\alpha = (u_{\alpha,1}, u_{\alpha,2})^T$, $\mathbf{w}_\alpha = (w_{\alpha,1}, w_{\alpha,2})^T$ and $\varphi = (\varphi_1, \varphi_2)^T$, respectively. Equation (36) can thus be rewritten as

$$\begin{aligned} & \left(\frac{\partial \varphi_1}{\partial t}, w_{\alpha,1}\right) + \left(\frac{\partial \varphi_2}{\partial t}, w_{\alpha,2}\right) + \left(\frac{\partial}{\partial x}(h_\alpha \varphi_1), \kappa_\alpha\right) + \left(\frac{\partial}{\partial y}(h_\alpha \varphi_2), \kappa_\alpha\right) + \left(u_{\alpha,1} \frac{\partial \varphi_1}{\partial x}, \alpha w_{\alpha,1}\right) \\ & + \left(u_{\alpha,2} \frac{\partial \varphi_1}{\partial y}, \alpha w_{\alpha,1}\right) + \left(u_{\alpha,1} \frac{\partial \varphi_2}{\partial x}, \alpha w_{\alpha,2}\right) + \left(u_{\alpha,2} \frac{\partial \varphi_2}{\partial y}, \alpha w_{\alpha,2}\right) + \left(\varphi_1 \frac{\partial u_{\alpha,1}}{\partial x}, \alpha w_{\alpha,1}\right) \\ & + \left(\varphi_2 \frac{\partial u_{\alpha,1}}{\partial y}, \alpha w_{\alpha,1}\right) + \left(\varphi_1 \frac{\partial u_{\alpha,2}}{\partial x}, \alpha w_{\alpha,2}\right) + \left(\varphi_2 \frac{\partial u_{\alpha,2}}{\partial y}, \alpha w_{\alpha,2}\right) = (g_{1,1}, \varphi_1) + (g_{1,2}, \varphi_2), \end{aligned}$$

$g_{1,1}$ and $g_{1,2}$ denoting the x - and y -components of the density \mathbf{g}_1 . The dual momentum equation can now be obtained by suitably integrating by parts all the terms involving a time or a space derivative of φ and by collecting the terms involving φ_1 and φ_2 , respectively. We get

$$\begin{aligned} & \left(-\frac{\partial w_{\alpha,1}}{\partial t} - h_\alpha \frac{\partial \kappa_\alpha}{\partial x} - \frac{\partial}{\partial x}(\alpha u_{\alpha,1} w_{\alpha,1}) - \frac{\partial}{\partial y}(\alpha u_{\alpha,2} w_{\alpha,1}) + \alpha \frac{\partial u_{\alpha,1}}{\partial x} w_{\alpha,1} + \alpha \frac{\partial u_{\alpha,2}}{\partial x} w_{\alpha,2}, \varphi_1\right) \\ & + \int_{\Omega} (\varphi_1 w_{\alpha,1}) \Big|_0^T d\Omega + \left([h_\alpha \kappa_\alpha + \alpha u_{\alpha,1} w_{\alpha,1}] n_1 + \alpha u_{\alpha,2} w_{\alpha,1} n_2, \varphi_1\right)_{\partial\Omega} = (g_{1,1}, \varphi_1), \quad (38) \end{aligned}$$

and

$$\begin{aligned} & \left(-\frac{\partial w_{\alpha,2}}{\partial t} - h_\alpha \frac{\partial \kappa_\alpha}{\partial y} - \frac{\partial}{\partial x}(\alpha u_{\alpha,1} w_{\alpha,2}) - \frac{\partial}{\partial y}(\alpha u_{\alpha,2} w_{\alpha,2}) + \alpha \frac{\partial u_{\alpha,1}}{\partial y} w_{\alpha,1} + \alpha \frac{\partial u_{\alpha,2}}{\partial y} w_{\alpha,2}, \varphi_2\right) \\ & + \int_{\Omega} (\varphi_2 w_{\alpha,2}) \Big|_0^T d\Omega + \left(\alpha u_{\alpha,1} w_{\alpha,2} n_1 + [h_\alpha \kappa_\alpha + \alpha u_{\alpha,2} w_{\alpha,2}] n_2, \varphi_2\right)_{\partial\Omega} = (g_{1,2}, \varphi_2), \quad (39) \end{aligned}$$

where $\mathbf{n} = (n_1, n_2)^T$ is the unit outward normal to the boundary $\partial\Omega$ and $(\cdot, \cdot)_{\partial\Omega}$ denotes the integral on $\partial\Omega \times (0, T]$. Equations (38) and (39) can be compacted in a single equation *via* suitable differential operators as

$$\begin{aligned} & \left(-\frac{\partial \mathbf{w}_\alpha}{\partial t} - h_\alpha \nabla \kappa_\alpha - \nabla(\alpha \mathbf{w}_\alpha) \mathbf{u}_\alpha - \alpha (\nabla \cdot \mathbf{u}_\alpha) \mathbf{w}_\alpha + \alpha (\nabla \mathbf{u}_\alpha)^T \mathbf{w}_\alpha, \varphi\right) + \int_{\Omega} (\varphi \cdot \mathbf{w}_\alpha) \Big|_0^T d\Omega \\ & + \left([h_\alpha \kappa_\alpha + \alpha u_{\alpha,1} w_{\alpha,1}] n_1 + \alpha u_{\alpha,2} w_{\alpha,1} n_2, \varphi_1\right)_{\partial\Omega} \\ & + \left(\alpha u_{\alpha,1} w_{\alpha,2} n_1 + [h_\alpha \kappa_\alpha + \alpha u_{\alpha,2} w_{\alpha,2}] n_2, \varphi_2\right)_{\partial\Omega} = (\mathbf{g}_1, \varphi). \quad (40) \end{aligned}$$

Integrating by parts the continuity equation (37) with the same spirit, we get

$$\left(-\frac{\partial \kappa_\alpha}{\partial t} - g \nabla \cdot \mathbf{w}_\alpha - \mathbf{u}_\alpha \cdot \nabla \kappa_\alpha, \vartheta\right) + \int_{\Omega} (\kappa_\alpha \vartheta) \Big|_0^T d\Omega + \left(g \mathbf{w}_\alpha \cdot \mathbf{n} + \mathbf{u}_\alpha \cdot \mathbf{n} \kappa_\alpha, \vartheta\right)_{\partial\Omega} = (g_2, \vartheta). \quad (41)$$

Thus the differential form of the adapted dual problem turns out to be given by

$$\begin{cases} -\frac{\partial \mathbf{w}_\alpha}{\partial t} - h_\alpha \nabla \kappa_\alpha - \nabla(\alpha \mathbf{w}_\alpha) \mathbf{u}_\alpha - \alpha (\nabla \cdot \mathbf{u}_\alpha) \mathbf{w}_\alpha + \alpha (\nabla \mathbf{u}_\alpha)^T \mathbf{w}_\alpha = \mathbf{g}_1, & \text{with } (\mathbf{x}, t) \in \Omega \times [0, T), \\ -\frac{\partial \kappa_\alpha}{\partial t} - g \nabla \cdot \mathbf{w}_\alpha - \mathbf{u}_\alpha \cdot \nabla \kappa_\alpha = g_2, & \text{with } (\mathbf{x}, t) \in \Omega \times [0, T). \end{cases}$$

Concerning the neglected terms, the time dependent ones are known due to the initial and final conditions associated with the primal and the dual problem, respectively. In particular, the final condition for the dual problem will be always given by $\mathbf{w}_\alpha = \mathbf{0}$, $\kappa_\alpha = 0$. On the other hand, since we recognize in (36)–(37) the dual weak form dictated by the DWR approach, we should choose the primal and dual boundary conditions so that all the boundary terms in (40) and (41) are identically equal to zero. Moreover, notice that the weak formulation (36)–(37) is more appropriate than (40)–(41) in view of the numerical validation, no derivative of the L^∞ -function α being involved.

Remark 3.6. Among the main drawbacks of the adopted DWR approach, we underline the constraint to employ the same space \mathcal{W} for both the primal and the dual problems. This limitation becomes particularly cumbersome in the presence of hyperbolic problems (namely, in our case) due to the involved characteristic analysis (see Sect. 5 for further details). Such a bound can be overcome by suitably combining a Petrov-Galerkin approach together with the constrained optimization strategy characterizing the DWR theory [24]. This makes the primal and the dual spaces independent one from the other.

4. THE DISCRETIZATION SCHEME

At this stage, we are interested in the modeling error control only, *i.e.* we are assuming to replace in (35) the quantities \mathbf{u}_α and \mathbf{w}_α with sufficiently accurate approximations $\mathbf{u}_{h,\alpha}$ and $\mathbf{w}_{h,\alpha}$, respectively.

The time discretization of the shallow water equations turns out to be tricky. Several approaches have been proposed in the literature: from ADI-schemes [35], to explicit, semi-implicit and implicit methods [2, 36], from fractional step techniques [2, 8], to stabilized Runge-Kutta approaches [38].

In the sequel we move from the linearized form of system (23)

$$\begin{cases} \frac{\partial \mathbf{u}_\alpha}{\partial t} + \alpha (\mathbf{U}_\alpha \cdot \nabla) \mathbf{u}_\alpha + g \nabla h_\alpha = 0 & \text{with } (\mathbf{x}, t) \in Q, \\ \frac{\partial h_\alpha}{\partial t} + H_\alpha \nabla \cdot \mathbf{u}_\alpha + \mathbf{U}_\alpha \cdot \nabla h_\alpha = 0 & \text{with } (\mathbf{x}, t) \in Q, \end{cases} \quad (42)$$

\mathbf{U}_α and H_α being suitable values for the mean velocity and the total water depth, respectively [36]. Then the Crank-Nicolson discretization scheme is applied to (42) to get the coupled system

$$\begin{cases} \mathbf{u}_\alpha^{n+1} - \mathbf{u}_\alpha^n + \frac{\Delta t}{2} (\alpha (\mathbf{U}_\alpha \cdot \nabla) \mathbf{u}_\alpha^{n+1} + g \nabla h_\alpha^{n+1}) + \frac{\Delta t}{2} (\alpha (\mathbf{U}_\alpha \cdot \nabla) \mathbf{u}_\alpha^n + g \nabla h_\alpha^n) = 0 & \text{with } \mathbf{x} \in \Omega, \\ h_\alpha^{n+1} - h_\alpha^n + \frac{\Delta t}{2} (H_\alpha \nabla \cdot \mathbf{u}_\alpha^{n+1} + \mathbf{U}_\alpha \cdot \nabla h_\alpha^{n+1}) + \frac{\Delta t}{2} (H_\alpha \nabla \cdot \mathbf{u}_\alpha^n + \mathbf{U}_\alpha \cdot \nabla h_\alpha^n) = 0 & \text{with } \mathbf{x} \in \Omega, \end{cases}$$

with Δt the time discretization parameter. The linearization (42) is performed about the values $\mathbf{U}_\alpha = \mathbf{u}_\alpha^n$ and $H_\alpha = h_\alpha^n$. The choice of the Crank-Nicolson scheme is essentially dictated by the good non-dissipative features of such a method, *i.e.* by its energy conservation property. As alternative approach, one could skip the linearization step by directly applying the Crank-Nicolson scheme to the nonlinear system (23). However this would unavoidably lead to a further increase of the computational cost of the already expensive DWR procedure.

On the other hand, for the space discretization of the primal problem (30) we use a finite element scheme based on continuous affine functions [10], moving from a computational grid reasonably fine.

The same space-time scheme is adopted to discretize the dual problem (32). Notice that no linearization is required in such a case as the dual problem is, by definition, linear.

It is evident that the computational cost associated with the modeling error estimator (35) is high. This is essentially due to the reverse time scale characterizing the dual framework. This disease becomes more evident in the presence of a large time interval or when a small time step is employed. In more detail, according to the adaptive procedure pursued in the numerical validation, the whole time interval should be spanned four times, twice forward and twice backward, to get the value η_α in (35) (see Sect. 5.1 for further details). This suggests for a non-cheap numerical procedure, on the other hand coherent with the “philosophy” of an unsteady DWR approach.

Finally, one could be interested in combining the model adaption together with a suitable mesh adaptivity. An example of analysis taking into account both the discretization and the modeling errors is provided in [9]. Nevertheless only stationary problems are considered in such a case. The addition of a time-dependent mesh adaptivity, allowing for grid refinement moving with the wave field, would undoubtedly lead to a prohibitive computational cost as well as to the development of spurious reflected waves caused by the jump of the mesh size [5, 6, 20]. This justifies our interest in modeling error control only.

5. NUMERICAL ASSESSMENT

The aim of this section is twofold. Moving from the modeling error estimator η_α in (35), we first sketch the algorithm used to decide which model of the hierarchy (23) has to be solved at each time and on each mesh element K , so that a prescribed tolerance τ is guaranteed on the goal quantity $|\mathcal{F}(U_1) - \mathcal{F}(U_\alpha)|$. Then we validate this algorithm on some numerical test cases related to standard hydrodynamic configurations such as a closed basin, a channel with an obstacle or a river bifurcation.

5.1. The adaptive procedure

Let us consider a fixed space-time partition of the computational domain Q . With this aim, let us introduce a conforming triangulation \mathcal{T}_h of $\bar{\Omega}$ into N_h triangles K , and divide the time interval $(0, T)$ into N_t uniform subintervals I_j .

To start the model adaption procedure we need a reference primal and dual solution. In order to confine the total computational cost, we begin by discretizing the coarse primal and the coarse dual problems, represented by equations (30) and (32), respectively, for α identically equal to zero. An initial guess $\eta_\alpha = \eta_0$ is thus yielded for the following adaptive procedure: for any I_j ,

- 1) evaluate the estimator η_α on each triangle K of \mathcal{T}_h via a suitable *localization* strategy, thus yielding the local modeling error estimator $\eta_{\alpha, K}^j = \eta_\alpha|_{K \times I_j}$;
- 2) then:
 - a) if $|\eta_{\alpha, K}^j| > \frac{\tau}{N_h N_t}$, set $\alpha|_{K \times I_j} = 1$, *i.e.* associate the fine model (24) with the element K of the space-time slab $S_j = \Omega \times I_j$;
 - b) if $|\eta_{\alpha, K}^j| \leq \frac{\tau}{N_h N_t}$, set $\alpha|_{K \times I_j} = 0$, *i.e.* discretize the coarse model (25) on the triangle K of S_j ;
- 3) discretize the adapted primal and dual problems (30) and (32), whose corresponding function α is the one identified at point 2);
- 4) evaluate the quantity η_α .

Notice that more loops 1)–4) are likely required in view of guaranteeing the global error $|\mathcal{F}(U_1) - \mathcal{F}(U_\alpha)|$ to be actually under the prescribed tolerance τ , in spite of the localization procedure. Moreover the check at the points 2a) and 2b) entails a space-time equidistribution of the modeling error on the elements of the mesh \mathcal{T}_h and for any time interval I_j .

The adaptive approach 1)–4) turns out to be reliable, even if very straightforward, as confirmed by the good quality of the numerical results in the next section.

Remark 5.1. The localization procedure used at point 1) simply exploits the additive property of the space-time integral understood by the scalar product (\cdot, \cdot) in the definition of η_α . We anticipate that such an approach will make the error estimator η_α a reliable but non-efficient adaptive tool (see Sect. 5).

We remark that the procedure 1)–4) above requires the whole time interval $(0, T)$ to be spanned four times, twice forward (coarse and adapted primal problem) and twice backward (coarse and adapted dual problem). This leads to an unavoidable memory requirement, the primal solution being actually stored at each time as providing the coefficients to the dual problem. This drawback is so far confined as the numerical tests deal with simple and 2D hydrodynamic configurations. Of course in view of more complex 3D simulations, we are aware that the memory storage is certainly an issue. The check-pointing technique suggested in [19] could be a useful alternative.

As first attempt to reduce the memory storage and the computational cost characterizing the approach 1)–4), we replace the estimator η_α by the new one

$$\tilde{\eta}_\alpha = \rho_M(U_\alpha)(Z_0) = -((\mathbf{u}_\alpha \cdot \nabla)\mathbf{u}_\alpha, (1 - \alpha)\mathbf{w}_0), \quad (43)$$

the time interval being spanned now only three times. From a theoretical viewpoint, this strategy finds a justification as, according to a DWR approach, the dual problem essentially weights how the error propagates, while the quantitative information is provided by the primal problem.

5.2. The numerical test cases

We validate the adaptive procedure 1)–4) of the previous section moving from three different hydrodynamic configurations. The first one deals with the evolution of a Gaussian hill in a closed basin. In the second test case a solitary wave moving along a straight channel with an obstacle is simulated. Finally, in the last test case, we consider the motion of a solitary wave along a river bifurcation. The numerical code is based on MATLAB and employs a direct method to solve all the linear systems involved.

5.2.1. The Gaussian hill test case

A well-known instance of a Gaussian hill is provided by the shape taken by the water surface after a stone has been thrown into the water at rest.

Let the computational domain $\Omega = (-20, 20)^2 \subset \mathbb{R}^2$ be a closed squared basin with a side of 40. The reference water level is chosen equal to 5. As the Coriolis force is neglected, the Gaussian breaks and gives rise to a circular wave propagating from the point $(0, 0)$ towards the boundary of the domain. Then, as the basin is closed, the wave is reflected backward to the center of the domain. On the other hand, the dual solution coincides with the Gaussian hill rewind in time.

The adapted model (23) is completed with suitable initial and boundary conditions. In more detail, at the initial time $t = 0$, the profile of elevation

$$h_\alpha(x, y, 0) = e^{-0.25(x^2+y^2)},$$

describing the Gaussian centered at $(0, 0)$ and with unitary height, is assumed together with a velocity identically equal to zero. Concerning the boundary conditions, as we are in the presence of a solid boundary, we assign, on the whole $\partial\Omega$, the usual slip condition $\mathbf{u}_\alpha \cdot \mathbf{n} = 0$, which means that the flow does not cross the boundary but may move tangentially only [18]. The space \mathcal{W} in (30) is thus identified by the following choices: $\mathcal{V} \equiv H_*^1(\Omega) = \{\mathbf{v} \in [H^1(\Omega)]^2 : \mathbf{v} \cdot \mathbf{n} = 0 \text{ on } \partial\Omega\}$, $\mathcal{Z} = H^1(\Omega)$. This means that the boundary condition associated with the dual problem is still a slip condition for the velocity, *i.e.* $\mathbf{w}_\alpha \cdot \mathbf{n} = 0$ on the whole boundary $\partial\Omega$. Moreover, after suitably rewriting the boundary terms in the dual momentum and continuity equations (40) and (41) as

$$\left(h_\alpha \kappa_\alpha, \boldsymbol{\varphi} \cdot \mathbf{n}\right)_{\partial\Omega} + \left(\alpha \mathbf{u}_\alpha \cdot \mathbf{n}, \mathbf{w}_\alpha \cdot \boldsymbol{\varphi}\right)_{\partial\Omega} + \left(g \mathbf{w}_\alpha \cdot \mathbf{n} + \mathbf{u}_\alpha \cdot \mathbf{n} \kappa_\alpha, \vartheta\right)_{\partial\Omega},$$

we notice that the choice made for the primal and the dual boundary conditions makes this quantity identically equal to zero.

To discretize both the primal and the dual problems (30) and (32), we adopt the scheme of Section 4, moving from a quasi-uniform mesh of $N_h = 5536$ elements. The time step Δt is chosen equal to 0.1 while the final time is $T = 18$. Finally we identify the goal functional \mathcal{F} with the quantity

$$\mathcal{F}(U_1) = \mathcal{F}_{GH}^{kin, \Omega}(U_1) = \frac{1}{2} \int_0^T \int_{\Omega} |\mathbf{u}_1|^2 \, d\Omega \, dt,$$

that is with the *kinetic energy* of the fluid on the whole domain Q . A tolerance $\tau = 10^{-1}$ is demanded on the approximating value $\mathcal{F}_{GH}^{kin, \Omega}(U_\alpha)$. This choice is dictated by the value $\mathcal{F}_{GH}^{kin, \Omega}(U_1) = 5.0411$, which is of the order of unity.

Let us analyze the numerical results. Figure 2 shows the distribution of the areas corresponding to the fine model (dark zones) and to the coarse one (light zones) at eight different times. In more detail, at each time the adapted free-surface model (23) is solved on the whole domain Ω , the piecewise constant function α being identically equal to 1 in correspondence of the dark areas and equal to 0 in the light zones. In particular, both the breaking of the initial Gaussian hill and the generation of the reflected wave are detected by the error estimator $\tilde{\eta}_\alpha$.

The percentage of the mesh elements where the fine model is discretized is plotted in Figure 3 (left) as a function of time. The three maxima are reached at about $t = 7.5, 12.5$ and 16.5 , namely when the reflection of the wave, massive due to the restricted dimension of the basin, is more intense. Nevertheless, notice that the mean percentage of the fine triangles is *circa* 47%. As expected, if a larger domain is considered, the values of the maxima diminish, the reflection phase being less strong (see Fig. 3 (right), where a domain $\Omega = (-30, 30)^2$ is considered along with $T = 20$).

In Figure 4 the distribution of the local modeling error estimator $\tilde{\eta}_{\alpha, K}^j$, basic tool for the adaptive procedure of Section 5.1, is represented in correspondence with the times $t = 8, 12.5$ and 16.5 . A comparison between the plots of Figures 2 and 4 associated with the same times, shows that, as expected, the largest values of $\tilde{\eta}_\alpha$ are associated with the areas of the domain where the fine model is solved.

We can also verify the good non-dissipative features of the Crank-Nicolson scheme simply by analyzing the plot of the mean total water depth $\bar{h}_\alpha = \int_{\Omega} h_\alpha \, d\Omega / |\Omega|$ as a function of time, $|\Omega|$ denoting the measure of the computational domain (see Fig. 5). No dissipation is practically present, the corresponding percentage reduction being of 0.028%. Moreover, it can be checked that, while the percentage error between the fine total water depth h_1 and the adapted one h_α is about 0.001%, the percentage error between h_1 and the coarse total water depth h_0 is about 0.1%.

Due to the academic nature of this test case, we use it to make some assessment on the adopted numerical procedure. We first compare the value of the “original” estimator η_α in (35), derived *via* the rigorous error analysis of Section 3.1, together with the result provided by the estimator $\tilde{\eta}_\alpha$ defined in (43) in view of the numerical validation. The two values are very similar, being $\eta_\alpha = -1.3986 \times 10^{-4}$ and $\tilde{\eta}_\alpha = -1.3719 \times 10^{-4}$ with a corresponding percentage error equal about to 1.94%. This result supports the employment of the estimator $\tilde{\eta}_\alpha$ in the numerical validation.

As second goal, we analyze the sensitivity of the error estimator (43) with respect to the time step Δt . We compute the estimator $\tilde{\eta}_\alpha$ for two different values of Δt ($= 0.1$ and 0.05) and by making three different choices for the tolerance τ ($= 10^{-1}, 0.5 \times 10^{-1}, 10^{-2}$). The corresponding results are summarized in Tables 1 (left and right), where the values of the corresponding *effectivity index*, calculated as $E.I. = \tilde{\eta}_\alpha / (\mathcal{F}(U_1) - \mathcal{F}(U_\alpha))$, are also provided.

The values tabulated for $\tilde{\eta}_\alpha$ are largely below the prescribed tolerance: three orders of magnitude are gained with respect to the demanded accuracy τ . This means that the error estimator (43) is reliable but not efficient. However, since the effectivity index is always around one, the procedure turns out to be almost optimal with

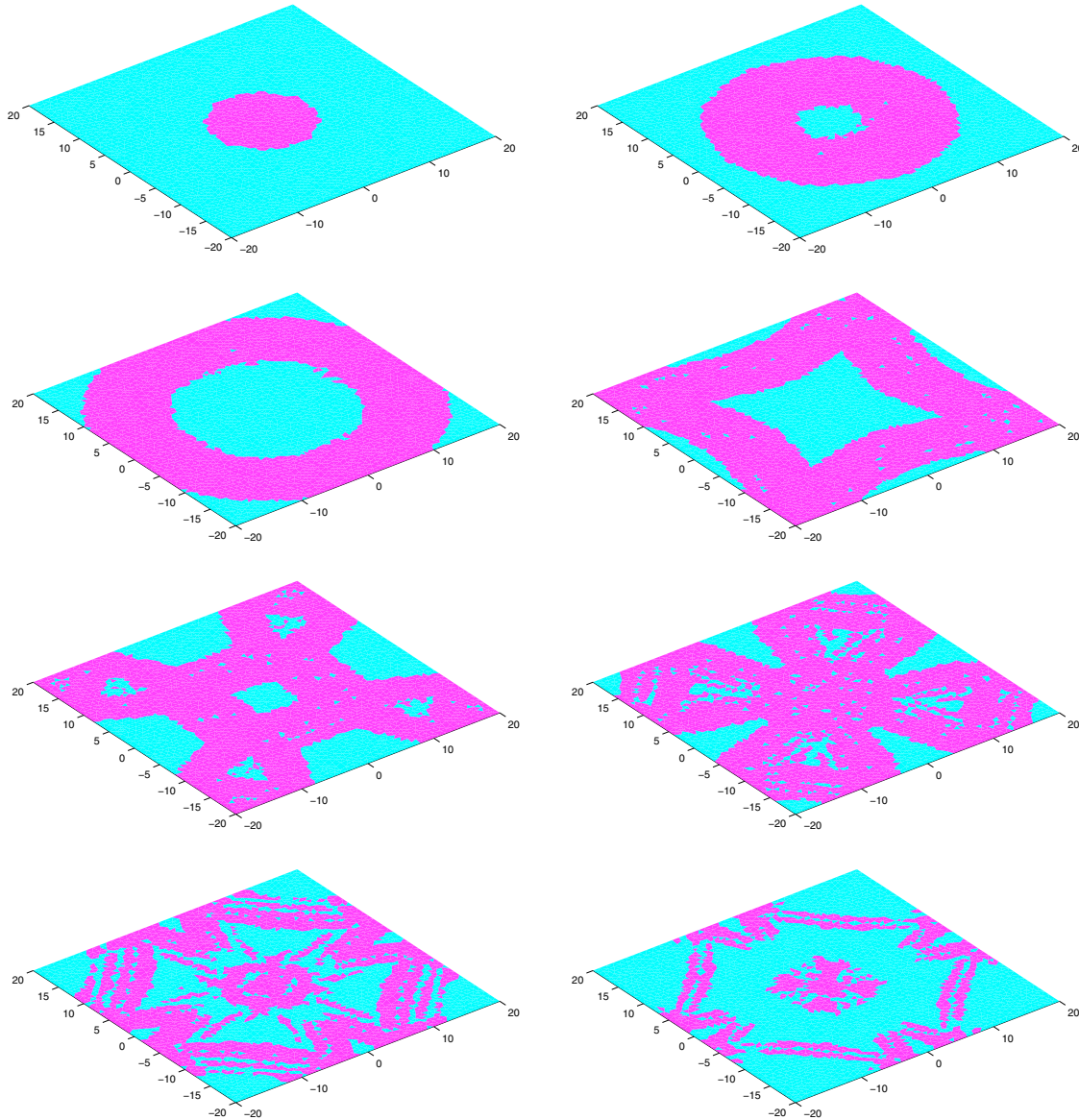


FIGURE 2. Distribution of the areas associated with the fine model (dark zones) and with the coarse model (light zones) for the Gaussian hill test case. Left-right, top-bottom: $t = 1, 5, 8, 12.5, 15, 16.5, 17.7$ and 18 .

respect to reliability. Moreover, the employment of a smaller time step does not guarantee an actual improvement of the performances of the adaptive procedure, though an increase of the computational cost is involved.

5.2.2. *The channel with an obstacle test case*

Let us consider the motion of a solitary wave moving rightward along a straight channel with an obstacle. We identify the computational domain $\Omega \subset \mathbb{R}^2$ with a channel 100 units long and 20 units wide, with a cylindrical pylon centered at $(x, y) = (30, 10)$ and with a radius $r = 4$. The horizontal sides together with the boundary of the obstacle are identified with the rigid walls of the channel. The reference water level is chosen equal to 5.

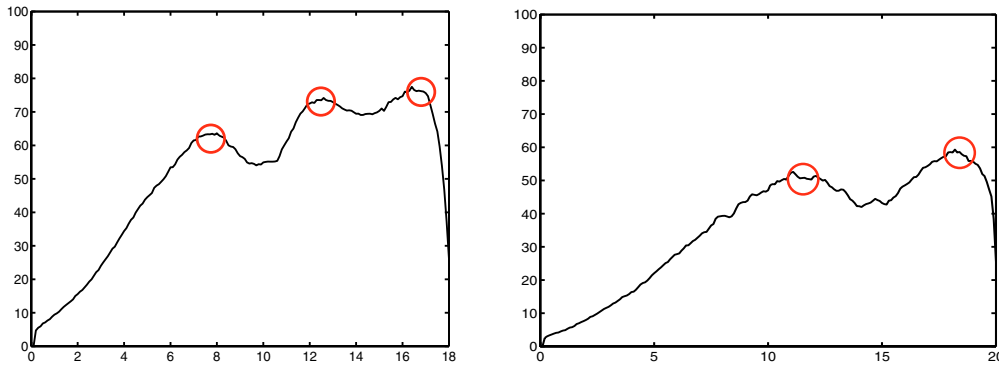


FIGURE 3. Time evolution of the percentage of mesh triangles associated with the fine model for the Gaussian hill test case: $\Omega = (-20, 20)^2$ on the left, $\Omega = (-30, 30)^2$ on the right.

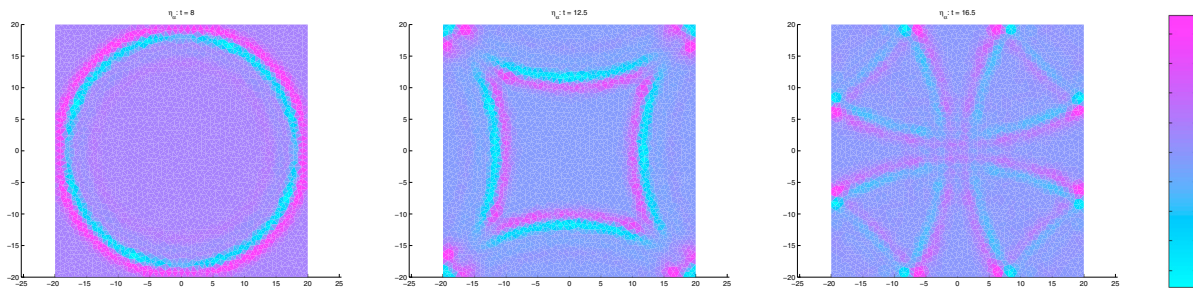


FIGURE 4. Distribution of the local modeling error estimator $\tilde{\eta}_{\alpha,K}^j$ at the times $t = 8$ (left), $t = 12.5$ (middle) and $t = 16.5$ (right) for the Gaussian hill test case.

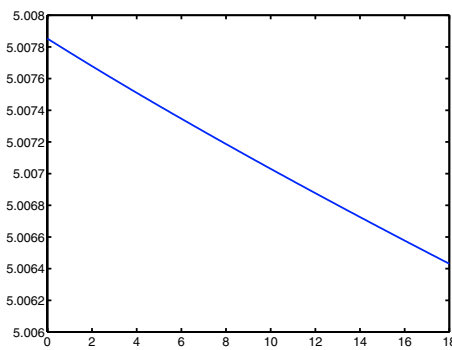


FIGURE 5. Time evolution of the mean total water depth \bar{h}_α for the Gaussian hill test case.

TABLE 1. Sensitivity of the error estimator $\tilde{\eta}_\alpha$ with respect to the time step Δt for the Gaussian hill test case: $\Delta t = 0.1$ on the left, $\Delta t = 0.05$ on the right.

| τ | $\tilde{\eta}_\alpha$ | E.I. |
|----------------------|--------------------------|------|
| 10^{-1} | -1.3719×10^{-4} | 1.05 |
| 0.5×10^{-1} | -7.9063×10^{-5} | 0.99 |
| 10^{-2} | -1.6686×10^{-5} | 1.34 |

| τ | $\tilde{\eta}_\alpha$ | E.I. |
|----------------------|--------------------------|------|
| 10^{-1} | -1.0275×10^{-4} | 1.15 |
| 0.5×10^{-1} | -5.1425×10^{-5} | 1.11 |
| 10^{-2} | -1.4216×10^{-5} | 1.18 |

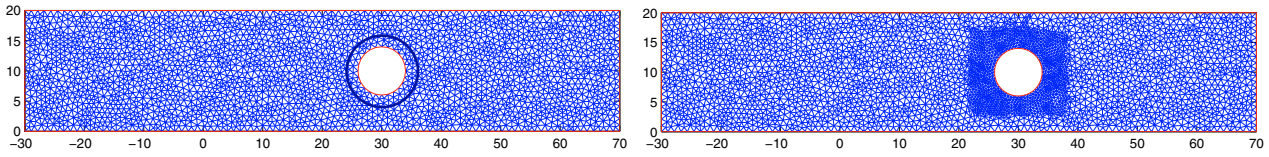


FIGURE 6. Channel with an obstacle test case: the quasi-uniform computational grid, where the control area γ is highlighted (on the left); the computational mesh locally refined around the pylon (on the right).

When the solitary wave strikes the obstacle, it breaks giving rise to a small reflected wave and to a large recirculation area, just behind the pylon itself [37]. On the contrary, the dual wave moves leftward, similar to the primal wave rewind in time.

The initial conditions associated with the adapted model (23) are

$$u_{\alpha,1}(x, y, 0) = \sqrt{11.76} \frac{0.2 \operatorname{sech}^2(\sqrt{0.15}(x - 10))}{5 + 0.2 \operatorname{sech}^2(\sqrt{0.15}(x - 10))}, \quad u_{\alpha,2}(x, y, 0) = 0, \quad (44)$$

$$h_{\alpha}(x, y, 0) = 0.2 \operatorname{sech}^2(\sqrt{0.15}(x - 10)) + 5,$$

i.e. the velocity and the elevation profile of a solitary wave centered along the line $x = 10$ and with height equal to 0.2. Concerning the boundary conditions, we are strictly bonded by the two following requirements: the functional space \mathcal{W} should be the same for both the primal and the dual problems; all the boundary terms in (40) and (41) have to be identically equal to zero (see Rem. 3.6).

The most practical choice to satisfy simultaneously these two constraints consists of imposing a slip condition on the whole boundary $\partial\Omega$, *i.e.* of handling the channel as a closed basin. This setting can be justified if we consider a channel, sufficiently long, so that the primal and the reflected wave do not have time enough to reach the open boundaries of the channel. This does not represent, maybe, the only possible choice but, no doubt, it is a reasonable compromise to guarantee the two requirements above while allowing for a physically sound numerical simulation. Thus the spaces \mathcal{V} and \mathcal{Z} identifying the functional space \mathcal{W} in (30) coincide with the ones adopted for the Gaussian hill test case, the dual problem also being provided with the slip condition $\mathbf{w}_{\alpha} \cdot \mathbf{n} = 0$ on the whole boundary $\partial\Omega$. To deal with a more realistic hydrodynamic configuration, a suitable extension of the DWR approach involving different functional spaces for the primal and the dual setting is highly desirable (see Rem. 3.6).

The space-time discretization scheme of Section 4 is used to approximate both the primal and the dual adapted problems. With this aim, we employ the quasi-uniform grid of $N_h = 5482$ triangles in Figure 6 (left) and a time step $\Delta t = 0.1$, $T = 17$ being the final time. For this test case, we make different choices for the goal functional \mathcal{F} . To assess the actual reliability of the provided *a posteriori* analysis, we first identify \mathcal{F} with a local (in space) functional. In more detail we select

$$\mathcal{F}(U_1) = \mathcal{F}_{Cyl}^{kin, \gamma}(U_1) = \frac{1}{2} \int_0^T \int_{\gamma} |\mathbf{u}_1|^2 \, d\Omega \, dt,$$

that is we are interested in controlling the kinetic energy of the fluid in an annular region $\gamma \subset \Omega$, of thickness 2, around the obstacle (see the highlighted area in Fig. 6, on the left). The tolerance τ is set to 10^{-1} , the value of $\mathcal{F}_{Cyl}^{kin, \gamma}(U_1)$ being 7.7048×10^{-1} .

The corresponding distribution of the fine and of the coarse areas at the times $t = 4.8, 8, 9.4, 11, 15$ and 17 is provided in Figure 7. The fine model is activated essentially in the zones surrounding the obstacle. During the first five times, the forward solitary wave together with a small backward wave are detected by the error

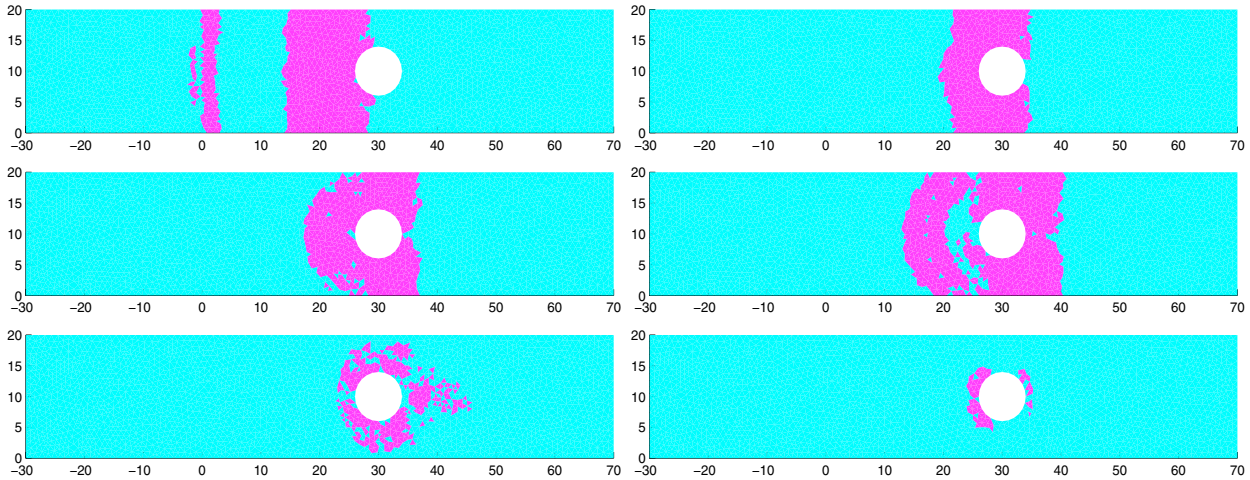


FIGURE 7. Distribution of the areas associated with the fine model (dark zones) and with the coarse model (light zones) for the channel with an obstacle test case and for the choices $\mathcal{F} = \mathcal{F}_{Cyl}^{kin, \gamma}$ and $\Delta t = 0.1$. Left-right, top-bottom: $t = 4.8, 8, 9.4, 11, 15$ and 17 .

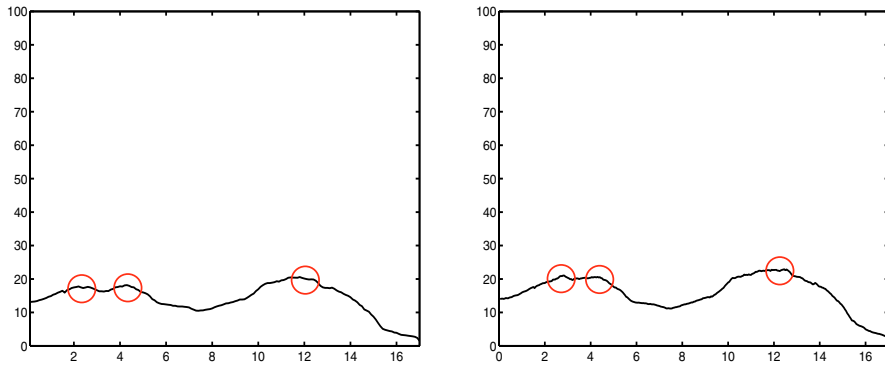


FIGURE 8. Time evolution of the percentage of mesh triangles associated with the fine model for the channel with an obstacle test case and for the choice $\mathcal{F} = \mathcal{F}_{Cyl}^{kin, \gamma}$: $\Delta t = 0.1$ on the left, $\Delta t = 0.05$ on the right.

estimator $\tilde{\eta}_\alpha$ as “carriers” of information to the target functional $\mathcal{F}_{Cyl}^{kin, \gamma}$. Then, for a small time interval, also the reflected wave, caused by the interaction of the primal wave with the pylon, is recognized by $\tilde{\eta}_\alpha$ (see the dark arch shaped area in front of the obstacle at $t = 11$). Finally, after $t = 15$, *i.e.* when the forward wave is sufficiently far from the pylon, a very reduced portion of the domain, confined around the obstacle, is still associated with the fine model. We remark that the first backward wave is not yielded by any interaction of the primal wave with the pylon (it would be present also without the obstacle!). The initial datum (44) is responsible for this feature, as allowing for both a forward and a backward wave.

In Figure 8 (left) we provide the time evolution of the percentage of the mesh elements where the fine model is solved: even when the global maximum is reached (during the interaction of the solitary wave with the obstacle), at most the 20% of triangles is associated with the fine model. In spite of this small number of fine elements, the approximation $\mathcal{F}_{Cyl}^{kin, \gamma}(U_\alpha) = 7.7053 \times 10^{-1}$ provides us with a value very close to the corresponding fine one $\mathcal{F}_{Cyl}^{kin, \gamma}(U_1)$.

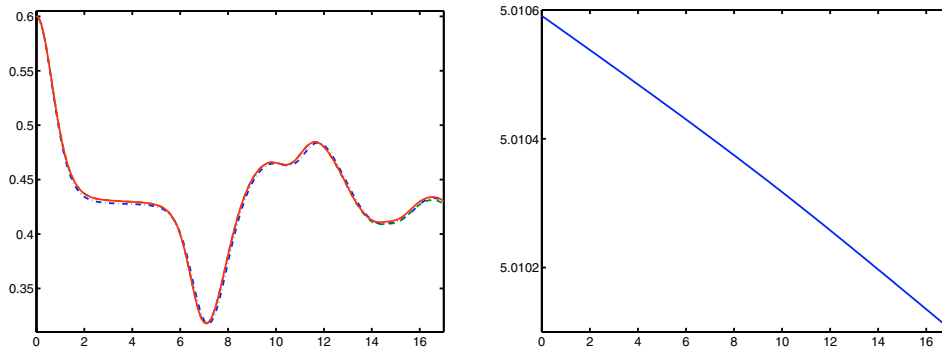


FIGURE 9. Channel with an obstacle test case, goal functional $\mathcal{F} = \mathcal{F}_{Cyl}^{kin, \gamma}$: evolution of the fine (solid line), adapted and coarse (dashed line) kinetic energy as a function of time (on the left); time evolution of the mean total water depth \bar{h}_α (on the right).

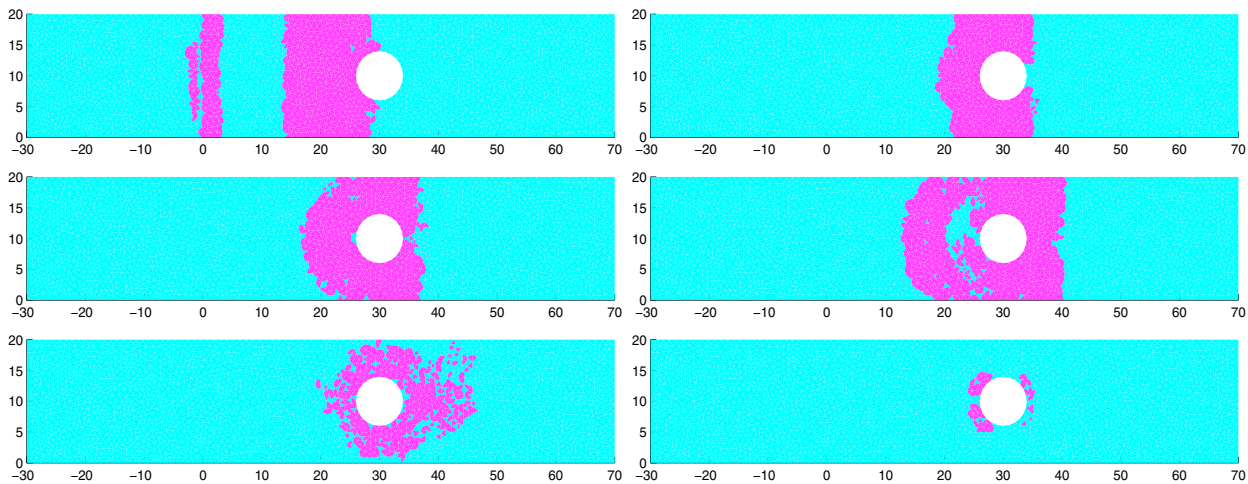


FIGURE 10. Distribution of the areas associated with the fine model (dark zones) and with the coarse model (light zones) for the channel with an obstacle test case and for the choices $\mathcal{F} = \mathcal{F}_{Cyl}^{kin, \gamma}$ and $\Delta t = 0.05$. Left-right, top-bottom: $t = 4.8, 8, 9.4, 11, 15$ and 17 .

The time evolution of the kinetic energy associated with the fine model together with the corresponding adapted and coarse quantities are plotted in Figure 9 (left). The solid line is adopted for the fine values while the dashed line displays the coarse kinetic energy. The plot associated with the adapted model is completely overlapped with the fine one. As expected, the adapted model provides us with an approximation more reliable with respect to what predicted by the coarse model.

The non-dissipativity of the Crank-Nicolson scheme is supported by the plot of the mean total water depth \bar{h}_α in Figure 9 (right), the percentage reduction being of 0.01%.

We exploit this test case to assess the sensitivity of the error estimator in (43) with respect to either the time step Δt or the computational mesh. First we analyze the behaviour of the estimator $\tilde{\eta}_\alpha$ by using two different time steps ($\Delta t = 0.1$ and $\Delta t = 0.05$), the computational grid, the target functional and the tolerance being the same as above. Figure 10 provides us with the distribution of the fine and coarse areas associated with the choice $\Delta t = 0.05$, at the same times collected in Figure 7 for $\Delta t = 0.1$.

TABLE 2. Sensitivity of the error estimator $\tilde{\eta}_\alpha$ with respect to the time step Δt for the channel with an obstacle test case and for the choice $\mathcal{F} = \mathcal{F}_{Cyl}^{kin,\gamma}$.

| | $\Delta t = 0.1$ | $\Delta t = 0.05$ |
|-------------------------|--------------------------|--------------------------|
| $\tilde{\eta}_\alpha$ | -4.0699×10^{-5} | -5.9273×10^{-6} |
| $\mathcal{F}(U_1)$ | 7.7048×10^{-1} | 7.7889×10^{-1} |
| $\mathcal{F}(U_\alpha)$ | 7.7053×10^{-1} | 7.7890×10^{-1} |
| E.I. | 0.94 | 0.57 |

TABLE 3. Sensitivity of the error estimator $\tilde{\eta}_\alpha$ with respect to the choice of the computational mesh for the channel with an obstacle test case and for the choice $\mathcal{F} = \mathcal{F}_{Cyl}^{kin,\gamma}$: quasi-uniform grid (on the left), locally refined grid (on the right).

| τ | $\mathcal{F}(U_\alpha)$ | $\tilde{\eta}_\alpha$ | E.I. | τ | $\mathcal{F}(U_\alpha)$ | $\tilde{\eta}_\alpha$ | E.I. |
|----------------------|-------------------------|--------------------------|------|----------------------|-------------------------|--------------------------|------|
| 10^{-1} | 7.7053×10^{-1} | -4.0699×10^{-5} | 0.94 | 10^{-1} | 7.5468×10^{-1} | -7.5231×10^{-6} | 2.53 |
| 0.5×10^{-1} | 7.7051×10^{-1} | -1.4195×10^{-5} | 0.65 | 0.5×10^{-1} | 7.5467×10^{-1} | 4.0702×10^{-6} | 2.08 |
| 10^{-2} | 7.7048×10^{-1} | 1.1396×10^{-6} | 0.46 | 10^{-2} | 7.5466×10^{-1} | -1.5949×10^{-6} | 0.88 |

The distribution of the triangles associated with the two models is very similar for the two time steps, even if a thickening, almost uniform, of the fine areas characterizes the choice $\Delta t = 0.05$. The same trend is derivable by comparing the time evolution of the percentage of the fine elements (see Fig. 8, right). The two plots essentially differ by a small shift factor, the mean percentage being slightly larger in the case $\Delta t = 0.05$. As already inferred from the Gaussian hill test case, the choice of a small time step seems a non-convenient strategy. The increase of the computational effort associated with a smaller Δt does not correspond to a reduced number of fine triangles.

The values of the estimator $\tilde{\eta}_\alpha$, of the target functional evaluated on the fine and on the adapted solution $\mathcal{F}_{Cyl}^{kin,\gamma}(U_1)$, $\mathcal{F}_{Cyl}^{kin,\gamma}(U_\alpha)$ and of the corresponding effectivity index E.I. are gathered in Table 2 for both the time steps. Notice that the different time step yields a change on the third significant digit of the goal value $\mathcal{F}_{Cyl}^{kin,\gamma}(U_1)$. The reliability and the non-efficiency of the estimator are confirmed by the values of $\tilde{\eta}_\alpha$ itself. As for the Gaussian hill test case we can again state that a smaller time step actually does not improve significantly the performances of our adaptive procedure.

To assess the effects of the computational mesh on the proposed modeling error analysis, we compute the error estimator $\tilde{\eta}_\alpha$ together with the approximate value $\mathcal{F}_{Cyl}^{kin,\gamma}(U_\alpha)$ and the corresponding effectivity index, moving from two different grids: the initial quasi-uniform mesh on the left of Figure 6 and a grid, of $N_h = 7185$ elements, refined only locally, *i.e.* in the region around the pylon where the kinetic energy has to be controlled (see Fig. 6 on the right). Three different choices are made for the tolerance τ , namely $\tau = 10^{-1}$, 0.5×10^{-1} and 10^{-2} , while the values $\Delta t = 0.1$ and $T = 17$ are preserved for the time step and the final time, respectively. The reference goal value for the locally refined mesh is $\mathcal{F}_{Cyl}^{kin,\gamma}(U_1) = 7.5466 \times 10^{-1}$.

The corresponding results are collected in Tables 3. The non-efficiency of the error estimator $\tilde{\eta}_\alpha$ is still more evident in the presence of the locally refined grid. Also the values of the effectivity index get worse. A first explanation can be identified in neglecting the contribution of the discretization error. On the other hand, as already pointed out, it is a well-known phenomenon that waves suffer spurious reflections in correspondence of discontinuities of the mesh-size (see, for example, [5, 6, 20]).

To stress the dependence of the “area-to-model” correspondence on the selected goal functional, we compare the distribution of the fine and coarse regions identified by three different functionals \mathcal{F} at the same times.

TABLE 4. Main quantities characterizing the model adaption driven by the three target functionals (45)–(47) for the channel with an obstacle test case.

| | $\mathcal{F} = \mathcal{F}_{Cyl}^{kin, \Omega}$ | $\mathcal{F} = \mathcal{F}_{Cyl}^{drag, \partial P}$ | $\mathcal{F} = \mathcal{F}_{Cyl}^{kin, T}$ |
|-------------------------|---|--|--|
| $\tilde{\eta}_\alpha$ | -6.7385×10^{-5} | 2.5580×10^{-5} | -5.4908×10^{-5} |
| $\mathcal{F}(U_1)$ | 7.4769 | 8.0522 | 3.7737×10^{-1} |
| $\mathcal{F}(U_\alpha)$ | 7.4770 | 8.0517 | 3.7741×10^{-1} |
| E.I. | 1.33 | 0.47 | 1.48 |

In more detail, we select as goal quantity a global value

$$\mathcal{F}(U_1) = \mathcal{F}_{Cyl}^{kin, \Omega}(U_1) = \frac{1}{2} \int_0^T \int_{\Omega} |\mathbf{u}_1|^2 \, d\Omega \, dt, \quad (45)$$

a value localized on a portion of the boundary $\partial\Omega$

$$\mathcal{F}(U_1) = \mathcal{F}_{Cyl}^{drag, \partial P}(U_1) = \int_0^T \int_{\partial P} g h n_1 \, d\gamma \, dt, \quad (46)$$

∂P denoting the contour of the pylon, and a quantity involving a point-wise value in time

$$\mathcal{F}(U_1) = \mathcal{F}_{Cyl}^{kin, T}(U_1) = \frac{1}{2} \int_{\Omega} |\mathbf{u}_1(\mathbf{x}, T)|^2 \, d\Omega. \quad (47)$$

In the first case we aim to control the kinetic energy of the fluid on the whole space-time domain; the choice (46) leads to control the so-called drag, that is the resultant force on the surface of the obstacle acting in the x -direction; the functional in (47) provides us with the value of the kinetic energy on the whole domain at the final time T . While the global functional (45) is a rather standard benchmark in view of a goal oriented analysis, the choice of a local (in space and/or time) functional represents, no doubt, the most challenging aim. Notice that, for numerical purposes, the functional $\mathcal{F}_{Cyl}^{drag, \partial P}$ is computed by rewriting it as an integral over Ω via a suitable Poisson problem (see, *e.g.*, [17]).

For all the three functionals the tolerance is chosen equal to 10^{-1} . The computational grid is represented by the uniform one in Figure 6, the time step is $\Delta t = 0.1$ and the final time is $T = 17$. Table 4 collects the associated values of the estimator $\tilde{\eta}_\alpha$, of the target quantities $\mathcal{F}(U_1)$ and $\mathcal{F}(U_\alpha)$, and of the associated effectivity index, while in Figures 11–13 the corresponding distributions of the fine and of the coarse areas are shown.

The non-efficiency of the error estimator is again evident from the values of $\tilde{\eta}_\alpha$. On the other hand, the approximations $\mathcal{F}(U_\alpha)$, obtained *via* the adapted solutions U_α , are very close to the corresponding target quantities $\mathcal{F}(U_1)$ in spite of a small value for the effectivity index associated with the functional $\mathcal{F}_{Cyl}^{drag, \partial P}$. Notice that the control of an integral over a curve as well as of a pointwise value is never an easy task and that our *a posteriori* analysis completely neglects the discretization error.

Concerning Figures 11–13, as expected the distribution of the mesh elements associated with the fine or with the coarse models changes according to the goal functional we are interested in. In more detail, both the controls of the kinetic energy detect the forward and the two backward waves as leading information to the functionals $\mathcal{F}_{Cyl}^{kin, \Omega}$ and $\mathcal{F}_{Cyl}^{kin, T}$, even if they are differently “tuned” (compare the thickness of the corresponding dark areas). The major difference is related to the time $t = 17$. The fine area is wider for the pointwise

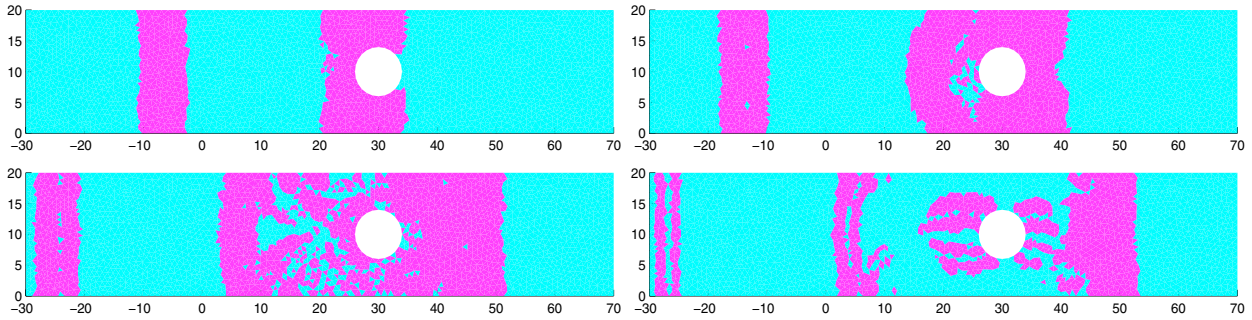


FIGURE 11. Distribution of the areas associated with the fine model (dark zones) and with the coarse model (light zones) for the channel with an obstacle test case and for the choice $\mathcal{F} = \mathcal{F}_{Cyl}^{kin, \Omega}$. Left-right, top-bottom: $t = 7.6, 10.7, 15.6$ and 17 .

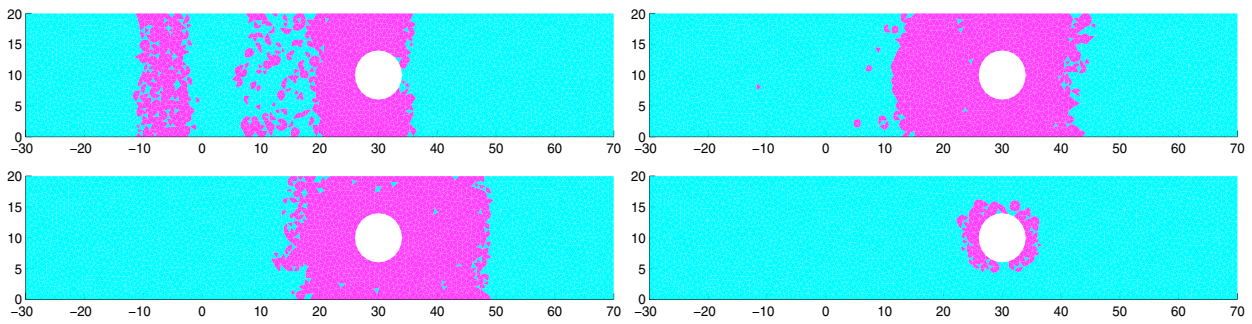


FIGURE 12. Distribution of the areas associated with the fine model (dark zones) and with the coarse model (light zones) for the channel with an obstacle test case and for the choice $\mathcal{F} = \mathcal{F}_{Cyl}^{drag, \partial P}$. Left-right, top-bottom: $t = 7.6, 10.7, 15.6$ and 17 .

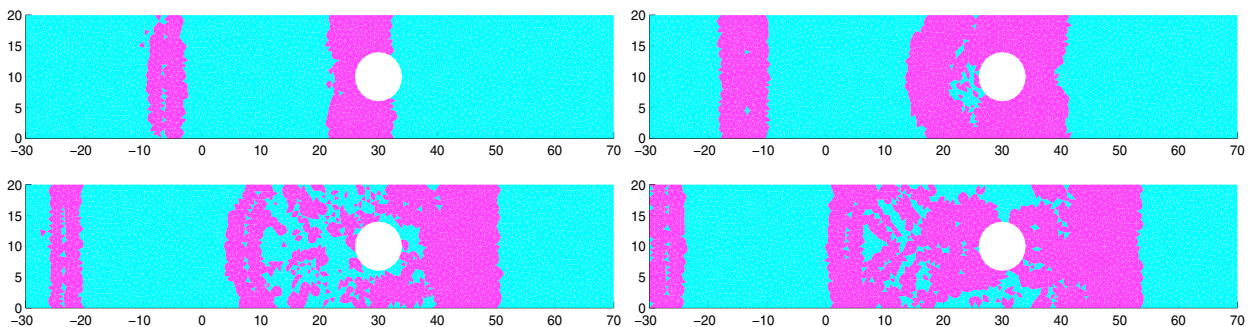


FIGURE 13. Distribution of the areas associated with the fine model (dark zones) and with the coarse model (light zones) for the channel with an obstacle test case and for the choice $\mathcal{F} = \mathcal{F}_{Cyl}^{kin, T}$. Left-right, top-bottom: $t = 7.6, 10.7, 15.6$ and 17 .

functional $\mathcal{F}_{Cyl}^{kin, T}$. This is probably related to the cancellation of the contribution of certain space-time cells implied by the integration over the whole space-time domain. On the contrary, the complex configuration where the two reflected waves coexist with the primal one and with other smaller waves reflected by the horizontal boundaries of the channel is wholly captured by the functional $\mathcal{F}_{Cyl}^{kin, T}$ (compare the distribution of the fine

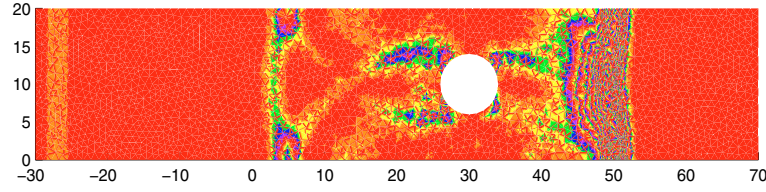


FIGURE 14. Distribution of the local “fine” kinetic energy at time T for the channel with an obstacle test case.

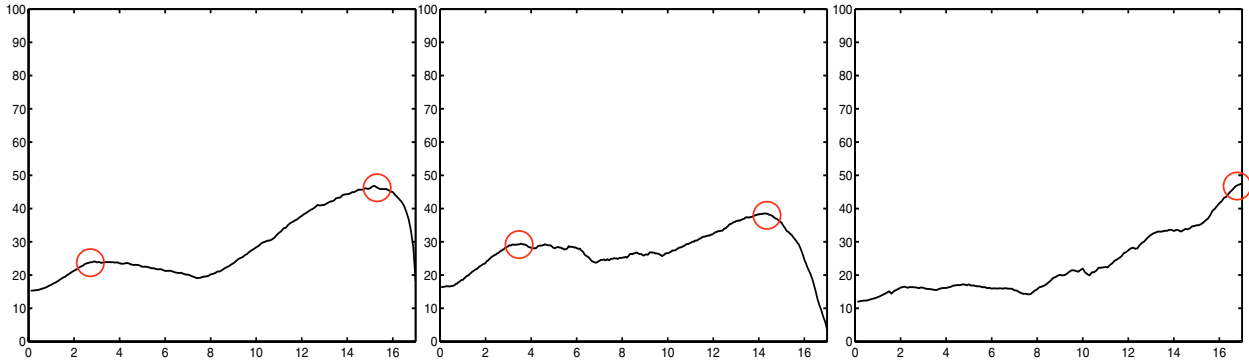


FIGURE 15. Time evolution of the percentage of mesh elements associated with the fine model for the channel with an obstacle test case: $\mathcal{F} = \mathcal{F}_{Cyl}^{kin, \Omega}$ (left), $\mathcal{F} = \mathcal{F}_{Cyl}^{drag, \partial P}$ (middle), $\mathcal{F} = \mathcal{F}_{Cyl}^{kin, T}$ (right).

areas in Figure 13, at time $t = 17$, with the plot of the local “fine” kinetic energy in Figure 14 associated with the final time T . The colormap is modified on purpose to emphasize the details of the wave dynamics).

The displacement of the fine and of the coarse areas dictated by the target functional $\mathcal{F}_{Cyl}^{drag, \partial P}$ is rather different. The forward and the first backward waves are initially identified by $\tilde{\eta}_\alpha$, even if the distribution of the fine triangles is quite scattered. After the primal wave strikes the pylon, all the region around the obstacle is uniformly marked for the fine model, so that neither the primal wave nor the reflected one are plainly distinguishable. When the interaction of the forward wave with the pylon reduces (approximately at $t = 15.5$), the fine region becomes smaller and smaller so that, at the final time T , very few elements are associated with model (24).

Overall, the fine problem is never solved on more than the 50% of the computational domain for all the three functionals (45)–(47) (see Fig. 15).

5.2.3. The river bifurcation test case

As last benchmark, let us consider the propagation of a solitary wave along a river bifurcation. The reference computational domain Ω is sketched in Figure 16. It represents a non-symmetric bifurcation with a length of 100 and a width, at the inflow, equal to 20. The curved horizontal boundaries are described by the equations

$$y = 5 \left(1 + \left(\frac{x-20}{50} \right)^2 \left(3 - \frac{2|x-20|}{50} \right) \right) + 2 \quad (\text{bottom boundary}),$$

$$y = 5 \left(-1 - \left(\frac{x-20}{50} \right)^2 \left(3 - \frac{2|x-20|}{50} \right) \right) + 2 \quad (\text{top boundary}),$$

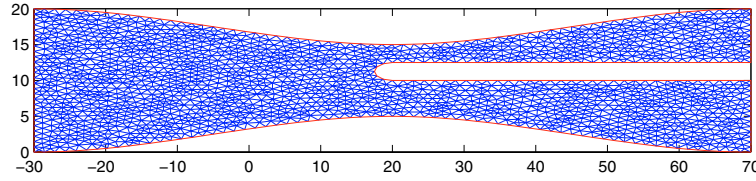


FIGURE 16. The river bifurcation test case: the quasi-uniform computational grid.

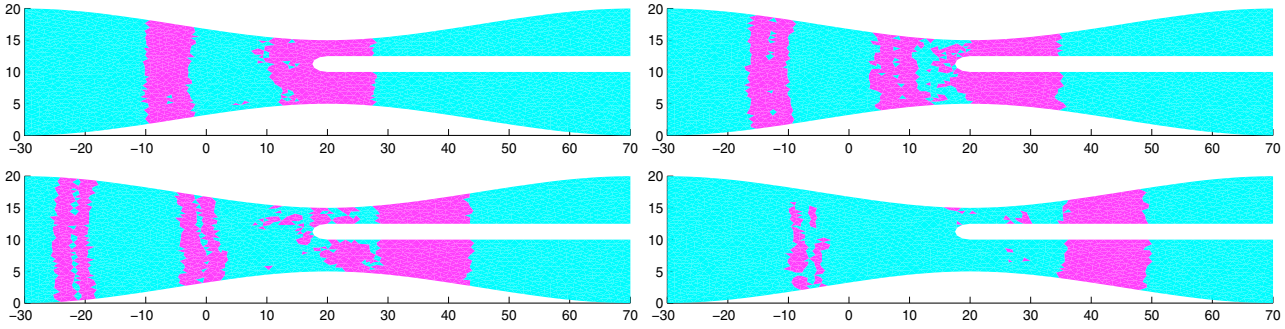


FIGURE 17. Distribution of the areas associated with the fine model (dark zones) and with the coarse model (light zones) for the river bifurcation test case and for the choice $\mathcal{F} = \mathcal{F}_{Bif}^{kin, \Omega}$. Left-right, top-bottom: $t = 6, 9.1, 12.9$ and 15.8 .

while the bifurcation is identified by a semi-ellipse centered at $(20, 11.25)$ and with semi-axes equal to 2.5 and 1.25 along the x and y direction, respectively. The non-symmetric shape of the bifurcation provides us with an actual two-dimensional phenomenon, unlike the channel with an obstacle test case. The reference water level is assumed equal to 5.

When the solitary wave reaches the bifurcation, it splits into two waves of different height, while a reflected wave moves backward. Nevertheless the interaction of the forward wave with the bifurcation is less strong than the one with the obstacle, no recirculation occurring in such a case. On the contrary, the dual wave consists, at the beginning, of two leftward waves of different height, merging each other after the bifurcation.

Both the initial and the boundary conditions are chosen coinciding with the ones adopted for the previous test case. The discretization of the primal and of the dual problems (30) and (32) is performed *via* the scheme proposed in Section 4, moving from the computational grid in Figure 16, consisting of $N_h = 4105$ elements, and from a time step $\Delta t = 0.1$, $T = 17$ being the final time.

The target quantity \mathcal{F} is first identified with the value of the kinetic energy on the whole space-time domain, *i.e.*

$$\mathcal{F}(U_1) = \mathcal{F}_{Bif}^{kin, \Omega}(U_1) = \frac{1}{2} \int_0^T \int_{\Omega} |\mathbf{u}_1|^2 \, d\Omega \, dt.$$

The tolerance τ is set to 10^{-1} .

Figure 17 provides us with the distribution of the areas where the fine and the coarse models are solved in correspondence of the times $t = 6, 9.1, 12.9$ and 15.8 . The results are rather similar to the ones associated with the channel with the obstacle test case for the same choice of the goal functional \mathcal{F} . Till about $t = 7$, the primal wave and the first backward one are highlighted by the estimator $\tilde{\eta}_\alpha$. Then, while the forward wave is splitting along the branches of the bifurcation, the reflected wave begins moving backward (see the two forward and the two backward waves at $t = 12.9$). Finally, after $t = 14.5$, the modeling estimator slowly loses the information

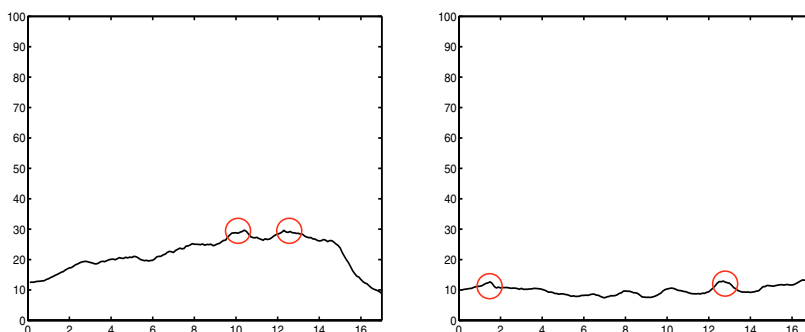


FIGURE 18. Time evolution of the percentage of mesh elements associated with the fine model for the river bifurcation test case: $\mathcal{F} = \mathcal{F}_{Bif}^{kin, \Omega}$ (left), $\mathcal{F} = \mathcal{F}_{Bif}^{kin, T}$ (right).

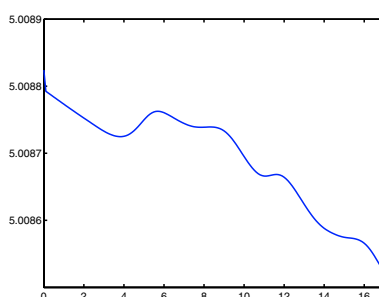


FIGURE 19. Time evolution of the mean total water depth \bar{h}_α for the river bifurcation test case and for the choice $\mathcal{F} = \mathcal{F}_{Bif}^{kin, \Omega}$.

provided by the backward waves, the waves along the branches remaining the only ones associated with the fine model.

The trend of the percentage of mesh elements associated with the fine model (24) is provided in Figure 18 (left) as a function of time. Notice that the fine problem is never solved on more than the 30% of triangles.

The non-dissipative property of the Crank-Nicolson scheme is corroborated by the trend of the mean total water depth \bar{h}_α (see Fig. 19). The percentage reduction is actually of 0.006% only.

To assess the sensitivity of $\tilde{\eta}_\alpha$ with respect to the tolerance τ , we repeat the same simulation by making different requirements on τ , chosen equal to 2×10^{-1} , 10^{-1} and 0.5×10^{-1} , respectively. These tolerances are selected taking into account the fine value $\mathcal{F}_{Bif}^{kin, \Omega}(U_1) = 4.3192$, which is of the order of unity. The corresponding values of the estimator $\tilde{\eta}_\alpha$, of the target functional evaluated on the adapted model and of the associated effectivity index are collected in Table 5. The quantities $\mathcal{F}_{Bif}^{kin, \Omega}(U_\alpha)$ represent a good approximation for the target value $\mathcal{F}_{Bif}^{kin, \Omega}(U_1)$ in spite of the non-efficiency of the modeling estimator (43) (again, about three orders of magnitude separate $\tilde{\eta}_\alpha$ and τ). On the other hand, the optimal values obtained for the effectivity index E.I. underline the reliability of the proposed error analysis.

To test the reliability of the estimator $\tilde{\eta}_\alpha$ with respect to the control of local quantities and in the presence of an actual 2D hydrodynamic configuration, we identify the target functional \mathcal{F} with the point-wise value in time

$$\mathcal{F}(U_1) = \mathcal{F}_{Bif}^{kin, T}(U_1) = \frac{1}{2} \int_{\Omega} |\mathbf{u}_1(\mathbf{x}, T)|^2 d\Omega.$$

TABLE 5. Sensitivity of the error estimator $\tilde{\eta}_\alpha$ with respect to the tolerance τ for the river bifurcation test case and for the choice $\mathcal{F} = \mathcal{F}_{Bif}^{kin,\Omega}$.

| τ | $\mathcal{F}(U_\alpha)$ | $\tilde{\eta}_\alpha$ | E.I. |
|----------------------|-------------------------|--------------------------|------|
| 2×10^{-1} | 4.3194 | -1.6031×10^{-4} | 1.02 |
| 10^{-1} | 4.3193 | -8.0588×10^{-5} | 0.95 |
| 0.5×10^{-1} | 4.3192 | -2.0127×10^{-5} | 1.07 |

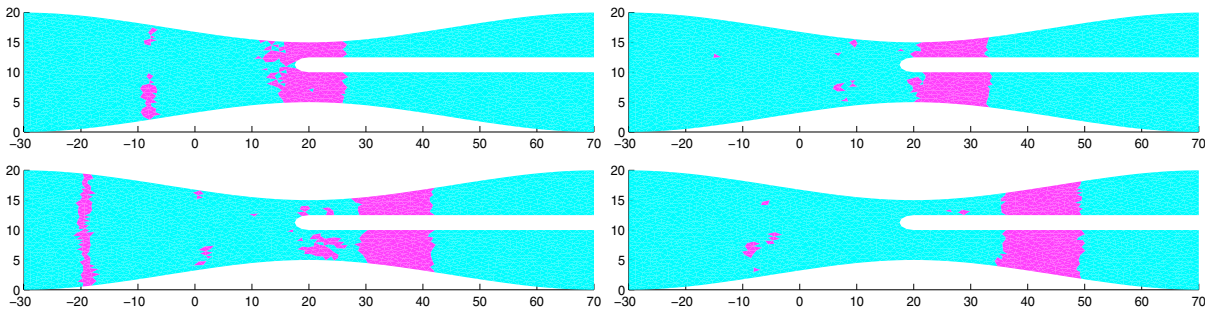


FIGURE 20. Distribution of the areas associated with the fine model (dark zones) and with the coarse model (light zones) for the river bifurcation test case for the choice $\mathcal{F} = \mathcal{F}_{Bif}^{kin,T}$. Left-right, top-bottom: $t = 6, 9.1, 12.9$ and 15.8 .

The choices made above for the tolerance τ , the computational grid, the time step Δt and the final time T are preserved.

The value predicted by the fine model for the goal quantity is $\mathcal{F}_{Bif}^{kin,T}(U_1) = 2.4317 \times 10^{-1}$, while the adapted model yields the approximation $\mathcal{F}_{Bif}^{kin,T}(U_\alpha) = 2.4333 \times 10^{-1}$. The estimator (43) still turns out to be reliable but non-efficient, $\tilde{\eta}_\alpha$ and E.I. being equal to -1.4851×10^{-4} and 0.92, respectively. Concerning the distribution of the fine and coarse areas provided in Figure 20 (at the same times as Fig. 17), we essentially remark that now both the backward waves are weakly detected by the modeling estimator. This likely finds a justification into the wave dynamics characterizing the river bifurcation, simpler compared with the one of the channel with an obstacle. For the local functional $\mathcal{F}_{Bif}^{kin,T}$, the percentage of triangles associated with the fine model (24) is never higher than 15% (see Fig. 18, right).

Remark 5.2. A heuristic check of the regularity assumptions made to deduce the modeling error estimator (35) from the exact relation (34) is performed in correspondence of all the three hydrodynamic configurations considered above. In more detail, in Figure 21 we compare the terms (I) and (II) in (34), the following common choice for the data being performed: $\mathcal{F} = \mathcal{F}^{kin,\Omega}$, $\tau = 10^{-1}$, $\Delta t = 0.1$, $T = 17$. An order of magnitude separates the two terms in the worst case, (I) being greater than (II) by two-three orders through the majority of time. We also remark that in all the test case considered the remainder term R in (21) is identically zero.

6. A LOOK BEHIND... AND A LOOK AHEAD

Moving from a hierarchy of Saint-Venant like models sharing the same functional space and boundary conditions, we have provided a reliable tool to estimate the target quantity $\mathcal{F}(u_{fine})$, u_{fine} being the solution of the most complex model of the hierarchy and \mathcal{F} the output functional of interest (e.g., kinetic energy, drag, a pointwise value). The idea is to evaluate $\mathcal{F}(u_{fine})$ within a prescribed accuracy by means of the computable quantity $\mathcal{F}(u_{adapted})$, i.e. via the so-called adapted solution which confines the approximation of the most complex model only to the areas of the domain largely influencing the goal quantity.

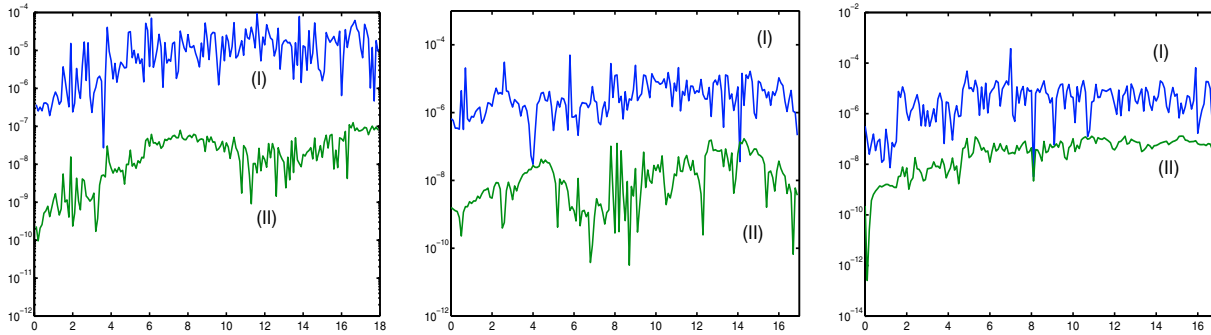


FIGURE 21. Comparison between the terms (I) and (II) in (34) for the Gaussian hill (left), the channel with an obstacle (middle) and the river bifurcation (right) test case as a function of time.

This aim has been achieved *via* a suitable *a posteriori* modeling error analysis developed in the DWR framework. In more detail, we have extended the approach in [9] to the (time-dependent) free-surface flows setting. Nevertheless, while in [9] only two models, the one at hand and the so-called reduced one, are considered, in our analysis, thanks to the introduction of a suitable piece-wise constant function α , we deal with the whole hierarchy of models, ranging from the fine to the coarse one. Moreover while in [9] the goal quantity is approximated by the reduced (coarse) solution, our approach exploits the adapted model.

A first issue associated with the unsteady setting is the time discretization of the dual problem, cumbersome as the time scale is reversed. This unavoidably demands for a memory requirement, the primal solution being actually stored at each time as providing the coefficients to the dual problem. This drawback remains confined till we limit our analysis to simple 2D hydrodynamic configurations, as in this paper. On the other hand, also the high computational cost of the whole adaptive procedure proposed in Section 5.1 can be pointed out as a limit of the proposed analysis. However, we underline that, when one is interested in approximating a functional of the solution, it sounds compulsory to resort to a suitable dual problem. Notice that the dual problem is always linear, namely cheaper to be approximated with respect to the primal one.

Several issues are left to be investigated in future works. First, we aim to move to the coupling of more than two and more heterogeneous models in view of the simulation of realistic hydrodynamic configurations [24]. In this respect, this paper is meant to found the bases for a more flexible and general analysis. Second, the matter of the memory storage is, no doubt, an issue in view of more complex (and possibly 3D) simulations. The check-pointing technique suggested in [19] looks as a reasonable remedy. Third, the choice of the boundary conditions for the dual problem represents another critical and scarcely addressed matter, especially in the presence of hyperbolic problems. This certainly deserves and will be subject of a thorough investigation [24]. Fourth, a clearer relationship between modeling and mesh adaptivity would be desirable too. Finally, the idea of an *a posteriori* modeling estimator can be undoubtedly made more incisive when dimensionally heterogeneous models are coupled. A first attempt in such direction has been provided in [4] and will be object of a forthcoming paper [12].

Acknowledgements. I thank Dr. S. Micheletti for his useful suggestions concerning the numerical computations and Professors A. Ern and F. Saleri for their useful comments. I would like also to acknowledge the two Referees for helping me to improve the paper.

APPENDIX – PROOF OF PROPOSITION 2.3

Let us consider the error on the goal quantity $\mathcal{F}(u_1) - \mathcal{F}(u_\alpha)$. Thanks to the relations (17) and (15) and by using the definition (16) of δL , we can rewrite it as

$$\begin{aligned}\mathcal{F}(u_1) - \mathcal{F}(u_\alpha) &= L(x_1) - L_\alpha(x_\alpha) = L(x_1) - L(x_\alpha) + \delta L(x_\alpha) \\ &= -d(u_\alpha)((1 - \alpha)z_\alpha) + \int_0^1 L'(x_\alpha + \lambda e)(e) \, d\lambda.\end{aligned}\tag{48}$$

The trapezoidal rule applied to the integral in (48) yields

$$\int_0^1 L'(x_\alpha + \lambda e)(e) \, d\lambda = \frac{1}{2} \{L'(x_1)(e) + L'(x_\alpha)(e)\} + R,$$

R being the remainder term defined in (21). Now, moving from equalities (5) and (15), and by exploiting the relation $L'_\alpha(x_\alpha)(y) = 0$, for any $y \in X$, we get

$$\begin{aligned}L'(x_1)(e) + L'(x_\alpha)(e) &= L'(x_\alpha)(e) = L'_\alpha(x_\alpha)(e) + \delta L'(x_\alpha)(e) \\ &= \delta L'(x_\alpha)(e) = -d(u_\alpha)((1 - \alpha)e_z) - d'(u_\alpha)(e_u, (1 - \alpha)z_\alpha),\end{aligned}$$

from which result (20) follows, after introducing the definitions (18) and (19) for the modeling residuals $\rho_M(u_\alpha)(z_\alpha)$, $\rho_M(u_\alpha)(e_z)$ and $\bar{\rho}_M(u_\alpha)(e_u, z_\alpha)$. \square

REFERENCES

- [1] R.L. Actis, B.A. Szabo and C. Schwab, Hierarchic models for laminated plates and shells. *Comput. Methods Appl. Mech. Engrg.* **172** (1999) 79–107.
- [2] V.I. Agoshkov, D. Ambrosi, V. Pennati, A. Quarteroni and F. Saleri, Mathematical and numerical modelling of shallow water flow. *Comput. Mech.* **11** (1993) 280–299.
- [3] V.I. Agoshkov, A. Quarteroni and F. Saleri, Recent developments in the numerical simulation of shallow water equations I: boundary conditions. *Appl. Numer. Math.* **15** (1994) 175–200.
- [4] M. Amara, D. Capatina-Papaghiuc and D. Trujillo, Hydrodynamical modelling and multidimensional approximation of estuarine river flows. *Comput. Visual. Sci.* **6** (2004) 39–46.
- [5] W. Bangerth and R. Rannacher, Adaptive finite element techniques for the acoustic wave equation. *J. Comput. Acoust.* **9** (2001) 575–591.
- [6] Z.P. Bažant, Spurious reflection of elastic waves in nonuniform finite element grids. *Comput. Methods Appl. Mech. Engrg.* **16** (1978) 91–100.
- [7] R. Becker and R. Rannacher, An optimal control approach to *a posteriori* error estimation in finite element methods, in *Acta Numerica 2001*, A. Iserles Ed., Cambridge University Press, Cambridge, UK (2001).
- [8] J.P. Benque, A. Haugel and P.L. Viollet, Numerical methods in environmental fluid mechanics, in *Engineering Applications of Computational Hydraulics*, M.B. Abbott and J.A. Cunge Eds., Vol. II (1982).
- [9] M. Braack and A. Ern, *A posteriori* control of modeling errors and discretization errors. *Multiscale Model. Simul.* **1** (2003) 221–238.
- [10] Ph. Ciarlet, *The Finite Element Method for Elliptic Problems*. North-Holland Publishing Company, Amsterdam (1978).
- [11] J.M. Cnossen, H. Bijl, B. Koren and E.H. van Brummelen, Model error estimation in global functionals based on adjoint formulation, in *International Conference on Adaptive Modeling and Simulation*, ADMOS 2003, N.-E. Wiberg and P. Díez Eds., CIMNE, Barcelona (2003).
- [12] A. Ern, S. Perotto and A. Veneziani, Finite element simulation with variable space dimension. The general framework (2006) (in preparation).
- [13] M. Feistauer and C. Schwab, Coupling of an interior Navier-Stokes problem with an exterior Oseen problem. *J. Math. Fluid. Mech.* **3** (2001) 1–17.

- [14] L. Formaggia and A. Quarteroni, Mathematical Modelling and Numerical Simulation of the Cardiovascular System, in *Handbook of Numerical Analysis*, Vol. XII, North-Holland, Amsterdam (2004) 3–127.
- [15] L. Formaggia, F. Nobile, A. Quarteroni and A. Veneziani, Multiscale modelling of the circulatory system: a preliminary analysis. *Comput. Visual. Sci.* **2** (1999) 75–83.
- [16] M.B. Giles and N.A. Pierce, Adjoint equations in CFD: duality, boundary conditions and solution behaviour, in *13th Computational Fluid Dynamics Conference Proceedings* (1997) AIAA paper 97–1850.
- [17] M.B. Giles and E. Süli, Adjoint methods for PDEs: *a posteriori* error analysis and postprocessing by duality. *Acta Numerica* **11** (2002) 145–236.
- [18] E. Godlewski and P.A. Raviart, *Numerical Approximation of Hyperbolic Systems of Conservation Laws*. Springer-Verlag, New York (1996).
- [19] A. Griewank and A. Walther, Revolve: an implementation of checkpointing for the reverse or adjoint mode of computational differentiation. *ACM T. Math. Software* **26** (2000) 19–45.
- [20] I. Harari, Reducing spurious dispersion, anisotropy and reflection in finite element analysis of time-harmonic acoustics. *Comput. Methods Appl. Mech. Engrg.* **140** (1997) 39–58.
- [21] J.L. Lions and E. Magenes, *Non-Homogeneous Boundary Value Problems and Applications*. Volume I. Springer-Verlag, Berlin (1972).
- [22] G.I. Marchuk, *Adjoint Equations and Analysis of Complex Systems*. Kluwer Academic Publishers, Dordrecht (1995).
- [23] G.I. Marchuk, V.I. Agoshkov and V.P. Shutyaev, *Adjoint equations and perturbation algorithms in nonlinear problems*. CRC Press (1996).
- [24] S. Micheletti and S. Perotto (2006) (in preparation).
- [25] E. Miglio, S. Perotto and F. Saleri, *A multiphysics strategy for free-surface flows*, *Domain Decomposition Methods in Science and Engineering*, R. Kornhuber, R.H.W. Hoppe, J. Périaux, O. Pironneau, O. Widlund, J. Xu Eds., Springer-Verlag, *Lect. Notes Comput. Sci. Engrg.* **40** (2004) 395–402.
- [26] E. Miglio, S. Perotto and F. Saleri, Model coupling techniques for free-surface flow problems. Part I. *Nonlinear Analysis* **63** (2005) 1885–1896.
- [27] J.T. Oden and S. Prudhomme, Estimation of modeling error in computational mechanics. *J. Comput. Phys.* **182** (2002) 469–515.
- [28] J.T. Oden and K.S. Vemaganti, Estimation of local modeling error and goal-oriented adaptive modeling of heterogeneous materials. I. Error estimates and adaptive algorithms. *J. Comput. Phys.* **164** (2000) 22–47.
- [29] J.T. Oden and K.S. Vemaganti, Estimation of local modeling error and goal-oriented adaptive modeling of heterogeneous materials. II. A computational environment for adaptive modeling of heterogeneous elastic solids. *Comput. Methods Appl. Mech. Engrg.* **190** (2001) 6089–6124.
- [30] J.T. Oden, S. Prudhomme, D.C. Hammerand and M.S. Kuczma, Modeling error and adaptivity in nonlinear continuum mechanics. *Comput. Method. Appl. M.* **190** (2001) 6663–6684.
- [31] A. Quarteroni and L. Stolicis, Heterogeneous domain decomposition for compressible flows, in *Proceedings of the ICFD Conference on Numerical Methods for Fluid Dynamics*, M. Baines and W.K. Morton Eds., Oxford University Press, Oxford (1995) 113–128.
- [32] A. Quarteroni and A. Valli, *Domain decomposition methods for partial differential equations*. Oxford University Press Inc., New York (1999).
- [33] M. Schulz and G. Steinebach, Two-dimensional modelling of the river Rhine. *J. Comput. Appl. Math.* **145** (2002) 11–20.
- [34] E. Stein and S. Ohnibus, Anisotropic discretization- and model-error estimation in solid mechanics by local Neumann problems. *Comput. Methods Appl. Mech. Engrg.* **176** (1999) 363–385.
- [35] G.S. Stelling, On the construction of computational models for shallow water equations. *Rijkswaterstaat Communication* **35** (1984).
- [36] C.B. Vreugdenhil, *Numerical Methods for Shallow-Water Flows*. Kluwer Academic Press, Dordrecht (1998).
- [37] G.B. Whitham, *Linear and Nonlinear Waves*. Wiley, New York (1974).
- [38] F.W. Wubs, *Numerical solution of the shallow-water equations*. CWI Tract, 49, F.W. Wubs Ed., Amsterdam (1988).